

Predicting the climate impact of aviation for en-route emissions: The algorithmic climate change function submodel ACCF 1.0 of EMAC 2.53

5 Feijia Yin¹, Volker Grewe^{1,2}, Federica Castino¹, Pratik Rao¹, Sigrun Matthes², Katrin Dahlmann², Simone Dietmüller², Christine Frömming², Hiroshi Yamashita², Patrick Peter², Emma Klingaman³, Keith Shine³, Benjamin Lührs⁴, Florian Linke⁴

¹ Delft University of Technology, Faculty of Aerospace Engineering, 2629HS, Delft, the Netherlands

² Deutsches Zentrum für Luft- und Raumfahrt, Institut für Physik der Atmosphäre, 82234 Wessling, Germany

³ University of Reading, Department of Meteorology, RG6 6AH Reading, United Kingdom

10 ⁴ Deutsches Zentrum für Luft- und Raumfahrt, Institut für Lufttransportsysteme, 21079 Hamburg, Germany

Correspondence to: Feijia Yin (F.yin@tudelft.nl)

Abstract Using climate-optimized flight trajectories is one essential measure to reduce aviation's climate impact. Detailed knowledge of temporal and spatial climate sensitivity for aviation emissions in the atmosphere is required to realize such a climate mitigation measure. The algorithmic Climate Change Functions (aCCFs) represent the basis for such purposes. This paper presents the first version of the Algorithmic Climate Change Function submodel (ACCF 1.0) within the European Center HAMburg general circulation model (ECHAM) and Modular Earth Submodel System (MESSy) Atmospheric Chemistry (EMAC) model framework. In the ACCF 1.0, we implement a set of aCCFs (version 1.0) to estimate the Average Temperature Response over 20 years (ATR20) resulting from aviation CO₂ emissions and non-CO₂ impacts, such as NO_x emissions (via ozone production and methane destruction), water vapour emissions, and contrail-cirrus. While the aCCF concept has been introduced in previous research, here, we publish a consistent set of aCCF formulas in terms of fuel scenario, metric, and efficacy for the first time. In particular, this paper elaborates on the contrail aCCF development, which has not been published before. ACCF 1.0 uses the simulated atmospheric conditions at the emission location as input to calculate the ATR20 per unit fuel burn, NO_x emitted, or per flown kilometer.

15

20

In this research, we perform quality checks of the ACCF 1.0 outputs in two aspects. Firstly, we compare climatological values calculated by ACCF 1.0 to previous studies. The comparison confirms that in the northern hemisphere between 150-300 hPa altitude (flight corridor), the vertical and latitudinal structure of NO_x-induced ozone and H₂O effects are well represented by the ACCF model output. The NO_x-induced methane effects increase towards lower altitudes and higher latitudes, which behaves differently from the existing literature. For contrail-cirrus, the climatological pattern of the ACCF model output corresponds with the literature, except that contrail-cirrus aCCF generates values at low altitudes near polar regions, which is caused by the conditions set up for contrail formation. Secondly, we evaluate the reduction of NO_x-induced ozone effects through trajectory optimization, employing the tagging chemistry approach (contribution approach to tag species according to their emission categories and to inherit these tags to other species during the subsequent chemical reactions). The simulation

25

30

35 results show that climate-optimized trajectories reduce the radiative forcing contribution from aviation NO_x-induced ozone compared to cost-optimized trajectories. Finally, we couple the ACCF 1.0 to the air traffic simulation submodel AirTraf version 2.0 and demonstrate the variability of the flight trajectories when the efficacy of individual effects is considered. Based on the one-day simulation results of a subset of European flights, the total ATR20 of the climate-optimized flights is significantly lower (roughly 50% less) than that of the cost-optimized flights, with the most considerable contribution from contrail cirrus. The CO₂ contribution observed in this study is low compared with the non-CO₂ effects, which requires further diagnosis.

1 Introduction

40 Civil aviation satisfies modern society's mobility needs and is an essential economic driver. Air transportation demand increases at around 4.4% per year and is forecast to maintain that growth for the next decades (Airbus, 2018). Though the global COVID-19 pandemic has put a tremendous challenge on the aviation industry, aviation (as a fundamental part of the modern world) will recover eventually. An example from the recent ICAO post-COVID forecast shows that the Revenue Passenger- Kilometres (RPK) is expected to grow at an annual average rate of 3.6% with a low and high range between 2.9% and 4.2% over the next three decades from 2018 to 2050.¹

On the other hand, the environmental impact of aviation is increasing at an evenly rapid pace. Aviation contributes 2.5% to global anthropogenic CO₂ emissions and is responsible for about 3.5% of global warming (Lee et al., 2021). This is because the non-CO₂ effects from aviation in the uppermost troposphere and lowermost stratosphere are as harmful to global climate change as CO₂ emissions (Lund et al., 2017). The non-CO₂ effects include ozone (O₃) formation and methane (CH₄) depletion (causing the primary mode ozone (PMO) and stratospheric water vapour (SWV) decrease) due to aviation NO_x emissions (Stevenson et al., 2004; Köhler et al., 2013; Myhre et al., 2007; Szopa et al., 2021; Terrenoire et al., 2022), contrail-cirrus (Heymsfield et al., 2010; Burkhardt and Kärcher, 2011; Schumann and Graf, 2013; Kärcher, 2018) and their alterations by aerosols direct and indirect effects (Kärcher et al., 2007; Penner et al., 2009; Myhre et al., 2013; Chen and Gettelman, 2016), and water vapour (H₂O) effect (Wilcox et al., 2012). Some recent studies investigated how COVID-19 affects aviation's climate impact per NO_x or contrails concerned. For instance, Voigt et al. (2022) conducted a measurement campaign to investigate atmospheric concentration changes. The authors observed a significant reduction in NO_x at cruise altitudes, contrail coverage, and the resulting radiative forcing. Furthermore, Gettelman et al. (2021) show that the effect of COVID-19 reductions in flights reduces contrail formation, which is aligned with the other study. However, due to spatial and seasonal variability of contrail radiative forcing, the annual mean contrail effective radiative forcing shows no significant changes.

50
55
60 Since aviation is expected to recover, it is still essential to address various climate effects of aviation with regard to their mitigation. The non-CO₂ effects depend not only on the emission quantity but also on the altitude, geographical location, time, and local weather conditions (e.g., Frömming et al., 2021). Therefore, it is possible to mitigate aviation's climate impact via

¹<https://www.icao.int/sustainability/Pages/Post-Covid-Forecasts-Scenarios.aspx>

operational measures to avoid climate-sensitive regions associated with non-CO₂ effects (Grewe et al., 2017b; Sridhar et al., 2011; Yin et al., 2018; Matthes et al., 2020).

65 Information on the climate-sensitive regions, i.e., areas where the non-CO₂ effects are significantly enhanced or reduced, is required to facilitate climate-optimized flight operations. In the earlier research within the EU-project REACT4C², Climate Change Functions (CCFs) were developed and implemented for flight trajectory optimization. The CCFs are 5D datasets (including longitude, latitude, altitude, time, and emission type) that describe the specific climate impacts, i.e., the average temperature change in K per flown kilometre or per emitted mass of the relevant species (NO_x and H₂O) locally. The high
70 fidelity CCFs were computed for eight representative weather situations (five winter patterns and three summer patterns classified by Irvine et al. (2013)) for the North Atlantic region (Frömming et al., 2021). Grewe et al. (2014a) discussed the development and verification procedure of CCFs thoroughly. Various application studies have demonstrated the effectiveness of the CCFs in climate-optimized trajectory calculations (Grewe et al., 2014b; Grewe et al., 2017b). These studies show promising mitigation potential when using CCFs as inputs for flight trajectory optimization (e.g., a 10% reduction in climate
75 impact for a 1% cost increase). One of the underlying challenges is that calculating these CCFs is computationally expensive. Thus, with the present computing performance, it is impossible to use CCFs for real-time calculation, which is necessary for future climate-optimized flight planning.

To this end, the previous research initiated development (Irvine, 2017; Matthes et al., 2017; van Manen and Grewe, 2019) and test (Rao et al., 2022) of the so-called algorithmic Climate Change Functions (aCCFs). The aCCFs are algorithmic
80 approximations of the high fidelity CCFs to represent the correlation of meteorological parameters (e.g., temperature and geopotential) at the time of emission and the respective average temperature change over a time horizon of 20 years (ATR20). Since the aCCFs are essentially mathematical approximations, they can be quickly implemented in Numerical Weather Prediction (NWP) models, thereby serving as a means of advanced meteorological information for flight trajectory planning. The ACCF submodel version 1.0 (ACCF 1.0) of the ECHAM5/MESSy Atmospheric Chemistry (EMAC) model is based on
85 the aCCFs version 1.0 (aCCFs 1.0). The ACCF 1.0 calculates the ATR20 from individual emissions and the contrail cirrus effect as a function of the online calculated local weather parameters in EMAC. One can use the ACCF 1.0 in two different ways: 1) to study the sensitivity of non-CO₂ effects (i.e., NO_x, H₂O, contrail-cirrus) to weather parameters; 2) to couple it with a flight planning tool (e.g., EMAC/AirTraf (Yamashita et al., 2016; Yamashita et al., 2020)) for climate-based routes optimization.

90 This paper elaborates on the modelling approach, the characteristics, and the application of ACCF 1.0. Please note that, for the first time, we show a consistent set of aCCFs formulas in terms of fuel scenario, metric, and efficacy (aCCFs 1.0). Due to the continuous development of aCCFs, we expect different versions of aCCFs to be released in the future. Accordingly, the ACCF submodel will be updated.

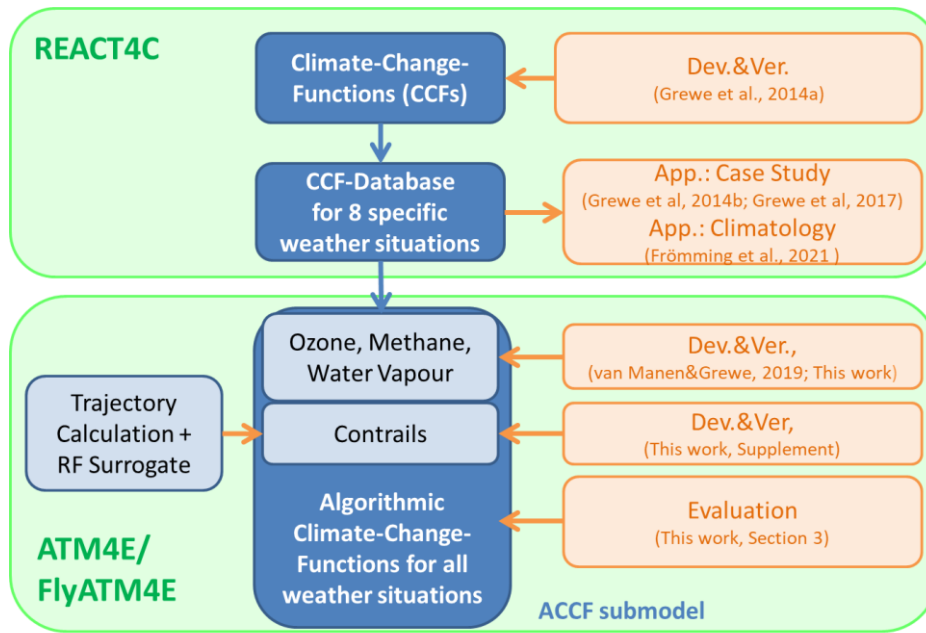
² www.react4c.eu

95 The structure of the paper follows that section 2 provides a roadmap of the ACCF 1.0 development focusing on different considerations when deriving the first version of contrail aCCFs and the NO_x and H₂O aCCFs. Section 3 presents an overview of ACCF 1.0, including the model components and the individual aCCFs formulas. The original correlations of the NO_x and H₂O aCCFs were derived in van Manen and Grewe (2019), whereas some coefficients in the equations are updated here for consistency. Furthermore, the contrail cirrus effect is explained in detail here (and in the supplement). In section 4, we evaluate the performance of the ACCF 1.0 outputs via two types of simulations. First, we compare the climatological aCCFs to other literature studies in terms of their latitudinal and vertical variability. Second, we use the tagging chemistry approach (contribution approach, Grewe et al., 2010 and Grewe et al., 2017a) to evaluate the reduction of NO_x-induced O₃ effect through climate-optimize flight trajectories based on the O₃ aCCF formula. Section 5 implements the ACCF 1.0 with the complete sets of aCCFs in the AirTraf 2.0 to demonstrate the usage of ACCF 1.0 for climate-optimized flight trajectories. It has to be noted that the two demonstration exercises are academic case studies, which don't intend to suggest an efficient implementation of such climate-optimized trajectories as we present here the extreme case of only considering ecological effects while completely ignoring economic effects in the optimisation (equivalent to a non-combined objective function). One could consider combining the cost and climate objectives in trajectory optimizations to identify eco-efficient flights (e.g., Matthes et al., 2022). Section 6 discusses further developments of aCCFs before concluding in section 7.

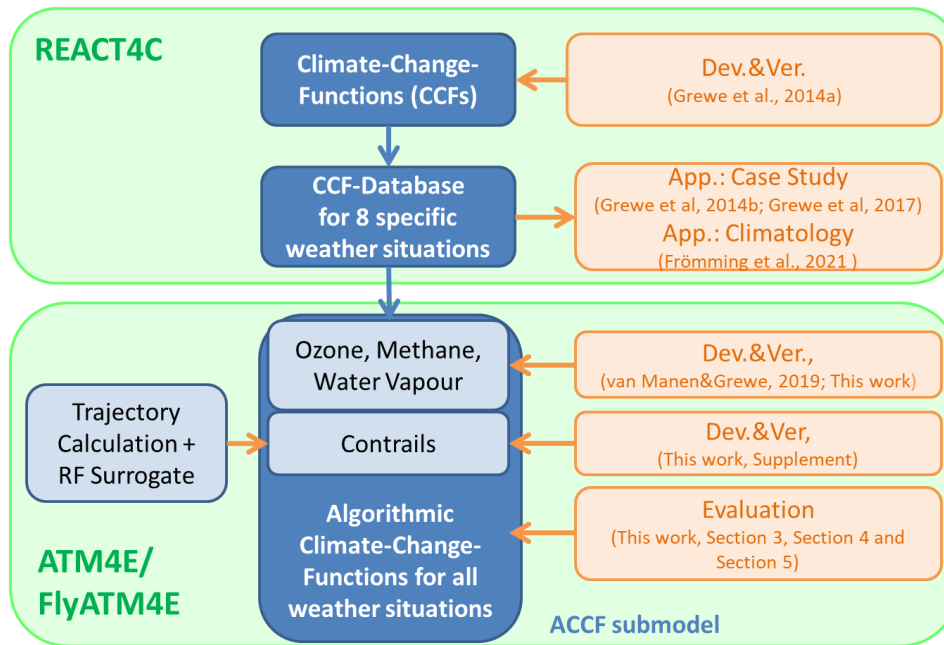
2 Roadmap of the MESSy ACCF 1.0 submodel development

110 The new MESSy submodel ACCF 1.0 consists of a set of aCCFs 1.0, which take relevant local meteorological data as inputs to calculate the ATR20 for a given emission or effect concerning contrails. As introduced above, the roadmap toward the ACCF 1.0 model involves multiple stages of work originating from different research projects. Figure 1 illustrates the development of the ACCF 1.0, including the previous research on the original CCFs development followed by the aCCFs approach, which is the core of the ACCF submodel. Meanwhile, we demonstrate the different processes between the CCFs and aCCFs model development. For instance, van Manen and Grewe (2019) analyzed the relation of weather data to different aviation climate effects, e.g., NO_x-induced O₃, NO_x-induced CH₄ and H₂O based on the CCFs datasets. Accordingly, the aCCFs were developed. Please note that though the aCCFs have been developed based on the CCF data, the formality is generalized beyond the weather pattern in CCFs. The work in Section 4.2 of this study attempts to evaluate the applicability of aCCFs by implementing the NO_x aCCFs on arbitrary day weather conditions concerning European flights. By evaluating the resulting emissions utilizing the EMAC model, the simulations confirmed the effectiveness of using the O₃ aCCF model for climate optimized trajectories to reduce the RF of aviation NO_x-induced O₃. Please see the details of the work in section 4.2 of this paper.

125 In this figure, we also demonstrate the major contributions of the current research. While the original CCFs and aCCFs have been developed and published in the previous research, the approach of developing contrails aCCFs is only made available in the current ACCF v1.0 manuscript as a supplement. Furthermore, one main effort of this research is to evaluate the quality of the aCCFs.



Dev.: Development; Ver.: Verification; App.: Application; RF: Radiative Forcing



Dev.: Development; Ver.: Verification; App.: Application; RF: Radiative Forcing

Figure 1 Overview of conceptual development and relevant projects (i.e., REACT4C, ATM4E, and FlyATM4E) leading to the algorithmic Climate Change Functions (aCCFs) and the ACCF submodel.

The individual CCFs, the basis of the aCCFs, were developed slightly differently. The CCFs of O₃, CH₄, and H₂O were calculated using a well-established modelling chain within EMAC (Jöckel et al., 2006; Jöckel et al., 2010). The model follows a multi-step approach starting with the simulation of the fate of emissions. The impact of pulse emission from a large number of time-region grid points is efficiently calculated by applying a Lagrangian transport scheme (i.e., following the air parcel).

135 The radiative forcing (RF) caused by these pulse emissions is computed using the online diagnostic of the EMAC radiation scheme. Grewe et al. (2014a) and Frömming et al. (2021) have described details of this approach.

For the contrail CCF, the Lagrangian trajectories were used to determine the lifetime of a contrail, the temperature, and the position along the lifetime of a contrail. The Lagrangian trajectories were computed using the ECMWF reanalysis data (ERA-Interim (Dee et al., 2011)) with winds input to a trajectory model (Methven, 1997). Accordingly, the contrail optical depth and solar zenith angle were calculated to obtain the contrail RF. The main discrepancy between contrail CCF and the other CCFs lies in the RF calculation. The contrail RF is calculated using the parametric model described by Schumann et al. (2012), which is different from the EMAC radiation scheme. Knowing the RF, to obtain the ATR20 value, the conversion from RF to ATR20 is calculated using the climate response model AirClim (Grewe and Stenke, 2008; Dahlmann et al., 2016) in a consistent way for all species considered, which was not the case in the earlier studies.

140
145 Based on the CCFs, the regression method was then applied to derive the aCCFs of O₃, CH₄, H₂O (van Manen and Grewe, 2019), and the contrail cirrus aCCFs (supplement of this paper). The CO₂ aCCF is a constant value, which is determined based on emission scenarios. Note that the values from van Manen and Grewe (2019) and Irvine et al. (2017, supplement to this publication) are updated by the formulas in the present study, as a more consistent conversion to ATR is employed, using slightly different response functions and consistent future scenarios for all species.

150 3 Overview of ACCF 1.0 submodel

3.1 Model description EMAC

ACCF 1.0 is a submodel of the global atmospheric-chemistry model EMAC. EMAC is a numerical chemistry-climate-model system that includes submodels describing the tropospheric and middle atmosphere processes and their interaction with oceans, land, and influences from anthropogenic emissions (Jöckel et al., 2010). It uses the second version of the Modular Earth
155 Submodel System (MESSy2 version 2.53; Jöckel et al. 2010) to connect computer codes generated from different institutions. The core atmospheric model is the 5th generation European Center Hamburg general circulation model (ECHAM5 version 5.3.02, Röckner et al. 2006). The model resolution used in the current study is T42L31ECMWF, corresponding to 2.8° by 2.8° in latitude and longitude and 31 vertical hybrid pressure levels up to 10 hPa. The temporal resolution is 12 minutes.

3.2 Submodel ACCF 1.0

160 Figure 2 illustrates the structure of ACCF 1.0 and its interactions with other EMAC submodels. The ACCF 1.0 includes two layers: the Sub-Model Interface Layer (SMIL) and the Sub-Model Core Layer (SMCL). The SMIL manages model input/output through the CHANNEL submodel (Jöckel et al., 2010). The SMCL is independent of other submodels and

contains the code to solve the relevant equations for the individual aCCFs. The input variables to calculate aCCFs in the ACCF submodel are either from the base model calculation (i.e., temperature, geopotential) or from the other EMAC submodels. For instance, the H₂O aCCF is a function of potential vorticity (PV) provided by the submodel TROPOP (Jöckel et al., 2006). The day-time contrail aCCF depends on the Outgoing Longwave Radiation (OLR) at the top of the atmosphere from the submodel RAD (Dietmüller et al., 2016). The potential contrail coverage (potcov) calculated from the submodel CONTRAIL (Frömming et al., 2014) is used to determine whether persistent contrails can form and may lead to a climate impact by contrails. The supplement of this paper includes a user manual of the submodel ACCF. It describes the namelist settings of the ACCF submodel and includes submodels necessary for coupling input/output variables.

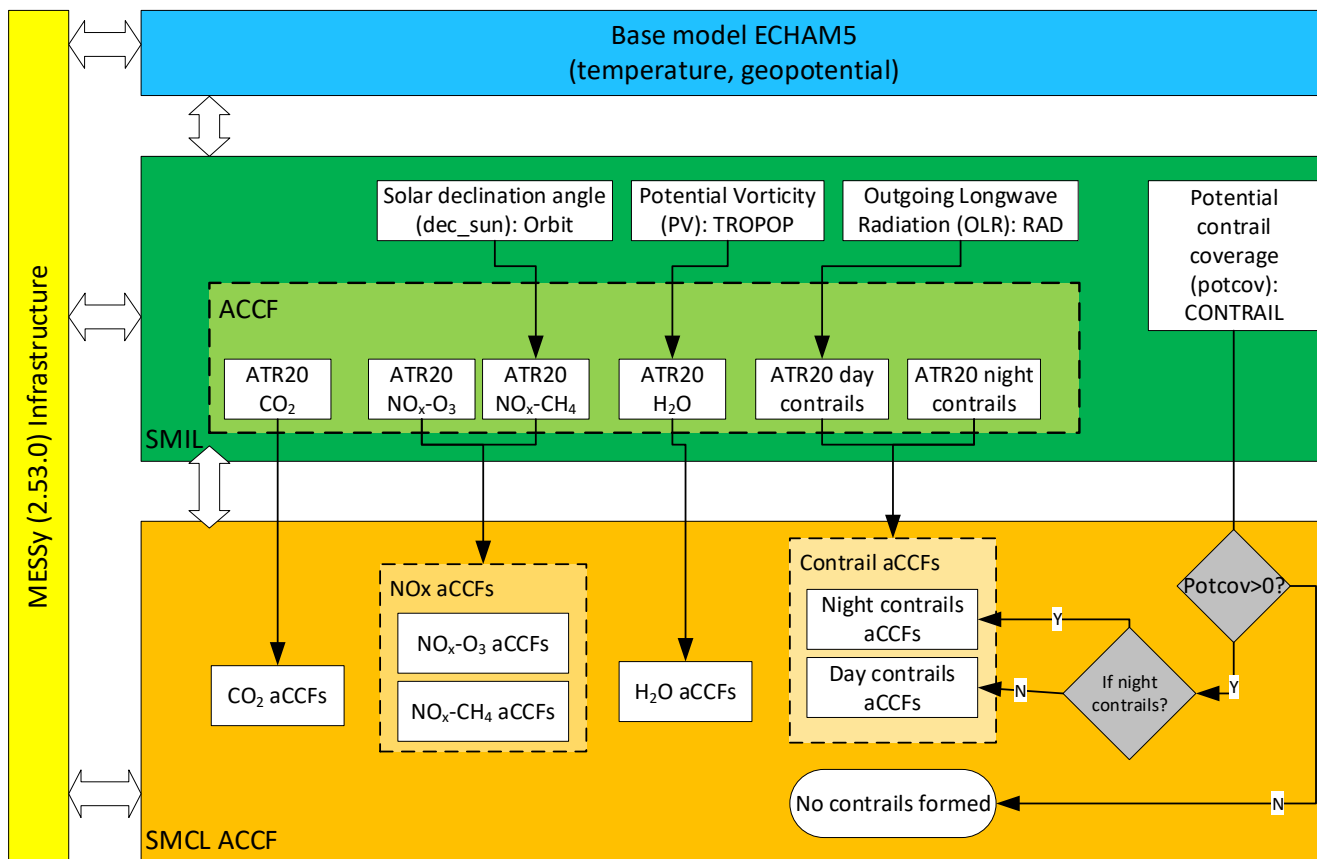


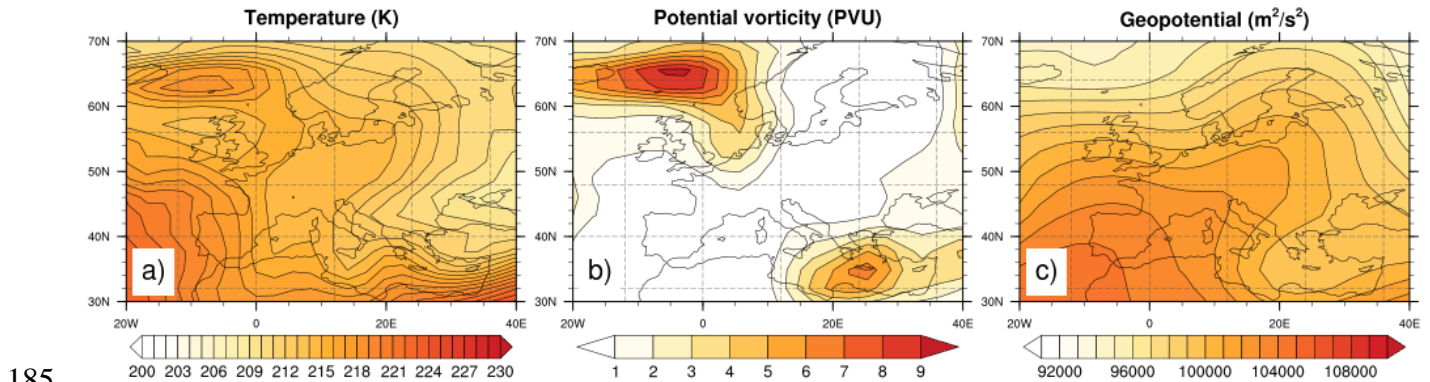
Figure 2 Overview of EMAC/ACCF submodel structure, the calculation process in the ACCF submodel, and its interaction with the other MESSy submodels. SMIL (submodel interface layer) and SMCL (submodel core layer) are components of MESSy coding standards.

175 3.3 Basic mechanisms of submodel ACCF 1.0

This section summarizes the formulas of aCCFs 1.0. For full details of the original derivation, the reader is referred to van Manen and Grewe (2019) and the supplement of this paper. The complete set of the aCCFs 1.0 computes the ATR20 of CO₂ emissions, H₂O emissions, NO_x emissions (forming O₃ and decreasing CH₄ + PMO), and day/night contrail-cirrus.

3.3.1 Synoptic on a selected day

180 The individual non-CO₂ aCCFs depend on weather parameters, e.g., temperature, geopotential, and potential vorticity. A one-day simulation on December 18th 2015 was performed to demonstrate such correlations. Figure 3 shows the geographical distribution of a) temperature, b) potential vorticity, and c) geopotential over Europe at the pressure level of 250 hPa on the same day. These parameters are calculated by running the EMAC model nudged towards the ERA-interim data and will be used to calculate the non-CO₂ aCCFs (see the following sections).



185 **Figure 3 Geographical distribution of a) Temperature (K); b) Potential Vorticity in standard potential vorticity unit (PVU, 1 PVU=10⁻⁶ K m² kg⁻¹ s⁻¹); c) Geopotential (m²/s²) over Europe at 250 hPa on December 18th 2015.**

3.3.2 CO₂ aCCF

CO₂ is a long-lived species, and hence, the climate impact of aviation's CO₂ depends only on the amount of CO₂ emitted. 190 Therefore, the CO₂ aCCF is calculated using the nonlinear climate–chemistry response model AirClim, assuming a 1 Tg fuel use in 2017. The CO₂ aCCF then represents the average temperature response of CO₂ for 2017-2036 in K/kg(fuel) (named P-ATR20_{CO2}). As a result, a constant value of 7.48e-16 K/kg(fuel) was obtained. For the same amount of emission in 2017, but with an annual growth rate according to a Business As Usual (BAU) future scenario as given by Grewe et al. (2021), the ATR20 for CO₂ (named F-ATR20_{CO2}) was 7.03e-15 K/kg(fuel). A conversion factor of 9.4 was derived from the P-ATR20_{CO2} 195 to F-ATR20_{CO2}.

3.3.3 NO_x induced aCCFs

The aviation NO_x emission (NO_x=NO+NO₂) leads to O₃ formation via a catalytic reaction. NO reacts with HO₂ forming NO₂. Due to photodissociation, NO₂ forms O(³P), leading to the O₃ formation. The O₃ formation, on the other hand, enhances the OH production (e.g., Grewe et al., 2017a), hence causing a shift of the OH/HO₂ ratio towards OH. The additionally formed 200 OH leads to the oxidation of CH₄.

Furthermore, the destruction of CH₄ leads to a reduced O₃ production rate as feedback to the O₃ concentration. This O₃ change is called primary mode ozone (PMO) (Wild et al., 2001). The effect of PMO is much smaller than the initial O₃ production. However, PMO has a longer lifetime (is bound to the CH₄ perturbation) than the initial O₃ production. Furthermore, because

205 of the CH₄ oxidation, less CH₄ enters the stratosphere, which again reduces the SWV. Since H₂O is a greenhouse gas, the decrease in SWV reduces the warming effect of H₂O (Myhre et al., 2007). The overall aviation-induced NO_x effects include the short-term O₃ increase and long-term CH₄ reduction (also CH₄-related PMO and SWV decrease). The current NO_x aCCF addresses the impact of short-term O₃ production and CH₄ destruction, and PMO reduction. SWV decrease is not taken into account because of its low magnitude. The corresponding formulas are presented below.

210 *NO_x-induced O₃-aCCF*

The earlier research showed the impact of weather patterns and related transport processes on the contribution of aviation NO_x emissions to O₃ and CH₄ concentrations (Grewe et al., 2017c, Frömming et al., 2021; Rosanka et al., 2020). For instance, Grewe et al. (2017c) and Frömming et al. (2021) showed that a unit NO_x emission within a high-pressure blocking situation leads to more O₃-induced RF than a NO_x emission west of this high pressure area because the transportation pathways differ significantly. Air parcels starting within the high-pressure system are transported to the tropics and lower altitudes, experiencing a more active chemical regime and faster O₃ production (Rosanka et al., 2020).

215 The analysis by van Manen and Grewe (2019) independently looked at correlations of CCFs data describing the atmospheric state (meteorological and chemical data) at the time of emission. They found the best correlation representing the impact of ozone changes caused by a local NO_x emission with the geopotential and temperature. This indicates that the weather regime at the time of emission essentially controls the air parcel's fate in which NO_x is emitted. Thereby, the O₃-aCCF in K/kg(NO₂) is developed based on temperature (T) in K and geopotential (Φ) in m²/s². For an atmospheric location (x, y, z) at time t with T = T(x, y, z, t) and Φ = Φ(x, y, z, t), the O₃-aCCF can be found in Eq. (1). Please note that the coefficients in Eq. (1) differ from those derived in van Manen and Grewe (2019) in order to have a consistent set of formulas representing ATR20 for a pulse emission scenario (P-ATR20). Based on this, other metrics, for instance, ATR20 for future emission scenarios (F-ATR20), can be derived (e.g., Table 1). For the same reasons, corrections are also applied for coefficients of methane formulas (Eq. (2)) and water vapour formulas (Eqn. (5)).

$$\begin{aligned}
 aCCF_{O_3}(T, \Phi) &= -2.64 \times 10^{-11} + 1.17 \times 10^{-13} \times T + 2.46 \times 10^{-16} \times \Phi - 1.04 \times 10^{-18} \times T \times \Phi \\
 aCCF_{O_3}(T, \Phi) &= \begin{cases} aCCF_{O_3}(T, \Phi) & \text{for } aCCF_{O_3} > 0 \\ 0 & \text{else} \end{cases} \quad (1) \\
 aCCF_{O_3} &\approx P\text{-ATR20}_{O_3}
 \end{aligned}$$

where P-ATR20_{O₃} is the ATR20 for a pulse emission.

230 Figure 4 a) shows an example of the O₃-aCCF in [K/kg(NO₂)] on December 18th 2015 over Europe at 250 hPa. The contour lines indicate the geopotential, and it is noticeable that the O₃-aCCF strongly follows the geopotential distribution. Overall, the changes in O₃ concentration caused by NO_x emissions have warming effects.

235 The analysis by van Manen and Grewe (2019) showed the highest correlation of the CH₄ response to NO_x emissions with geopotential and the mean incoming solar radiation, i.e., combining the initial transportation pathway with an indicator for both seasons and available incoming radiation. Therefore, the CH₄-aCCF in K/kg (NO₂) is based on geopotential (Φ) in m²/s² and incoming solar radiation at the top of the atmosphere as a maximum value over longitude (F_{in}) in W/m². For an atmospheric location (x, y, z) at time t with $\Phi = \Phi(x, y, z, t)$, the CH₄-aCCF can be found in Eq. (2).

$$\begin{aligned}
 aCCF_{CH_4}(\Phi, F_{in}) &= -4.84 \times 10^{-13} + 9.79 \times 10^{-19} \times \Phi - 3.11 \times 10^{-16} \times F_{in} + 3.01 \times 10^{-21} \times \Phi \times F_{in} \\
 aCCF_{CH_4}(\Phi, F_{in}) &= \begin{cases} aCCF_{CH_4}(\Phi, F_{in}) & \text{for } aCCF_{CH_4} < 0 \\ 0 & \text{else} \end{cases} \quad (2) \\
 aCCF_{CH_4} &\approx P-ATR20_{CH_4}
 \end{aligned}$$

where P-ATR20_{CH₄} represents the ATR20 for pulse emission, and F_{in} is calculated by Eq. (3)

$$\begin{aligned}
 F_{in} &= S \times \cos \theta, \text{ with } S = 1360 \text{ W/m}^2 \\
 \cos \theta &= \sin \varphi \times \sin d + \cos \varphi \times \cos d, \text{ and} \\
 d &= -23.44^\circ \times \cos(360/365 \times (N + 10))
 \end{aligned} \quad (3)$$

where S is the total solar irradiance, θ is the solar zenith angle, φ is latitude, and d is the declination angle, defined by the time of year via the day of the year N .

245 *NO_x-induced PMO-aCCF*

The effects of PMO and SWV decrease are not included in Eq. (2) but might be simply regarded as an offset of the CH₄-aCCF with a linear scaling factor (e.g., Skowron et al., 2013), as they are primarily driven by the CH₄ change. Here we apply a constant factor of 0.29 to the CH₄-aCCF calculated in Eq. (2) to account for the PMO effect (Dahlmann et al., 2016). The PMO-aCCF is then described by Eq. (4).

$$\begin{aligned}
 aCCF_{PMO} &= 0.29 \times aCCF_{CH_4} \\
 aCCF_{PMO} &\approx P-ATR20_{PMO}
 \end{aligned} \quad (4)$$

255 Figure 4 b) shows an example of the combined CH₄-CCF and PMO-aCCF in K/kg(NO₂) on December 18th 2015 over Europe at 250 hPa. The overlaid contour lines represent the geopotential on the same pressure level and time step. We can see that the decrease in CH₄ concentration caused by NO_x emissions has cooling effects. Here, the cooling effects are overcompensated by the warming effects of O₃. The overall effects of NO_x emissions are expected to be warming, as seen in Figure 4 c), which shows the summation of O₃-aCCF, CH₄-aCCF, and PMO-aCCF.

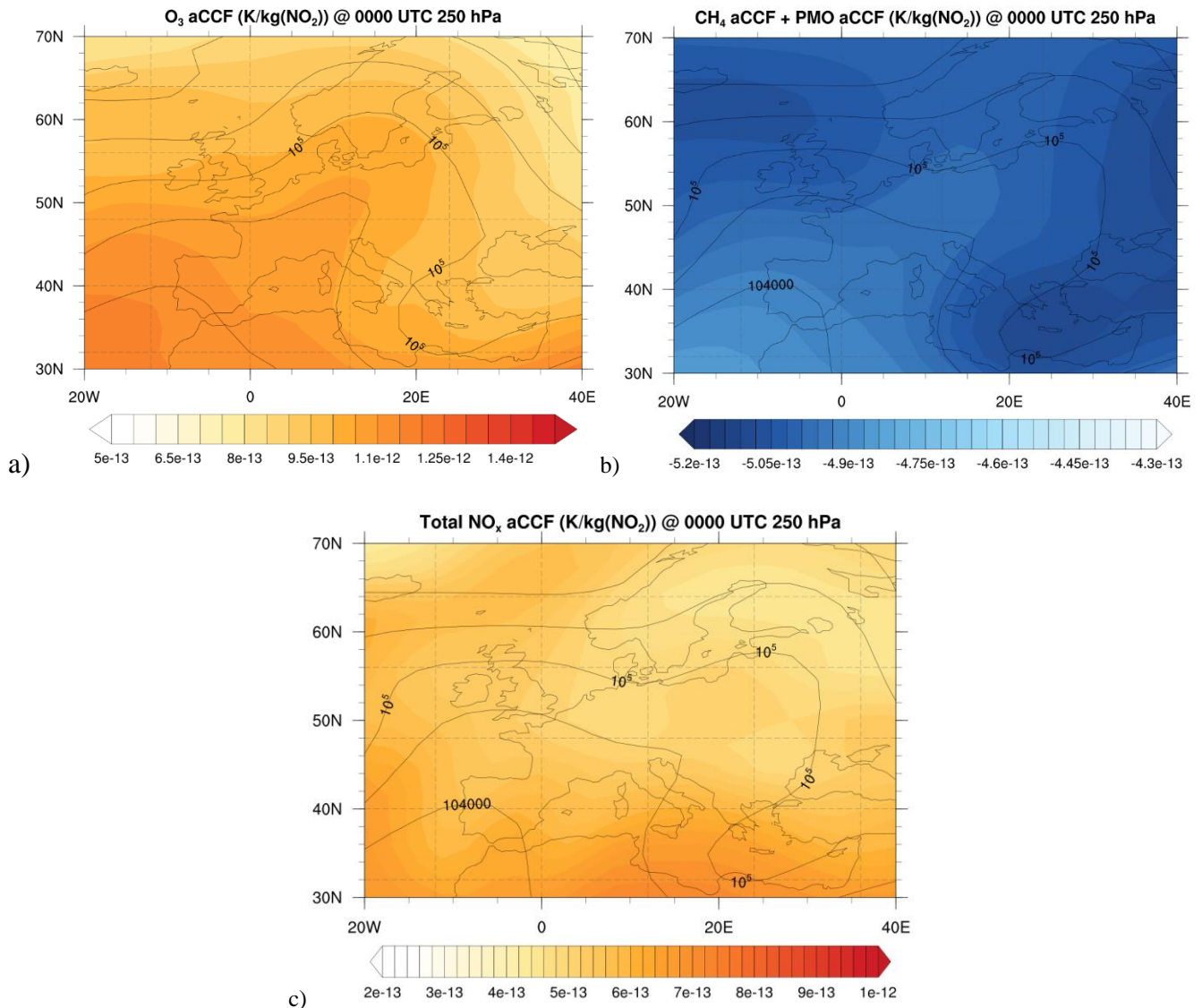


Figure 4 NO_x aCCF in $\text{K/kg}(\text{NO}_2)$ on December 18th 2015 at 250 hPa for: a) O_3 -aCCF; b) the combined CH_4 -aCCF and PMO-aCCF and c) the total NO_x aCCF (O_3 -aCCF + CH_4 -aCCF + PMO-aCCF). The black contour lines are geopotential in m^2/s^2 .

260

3.3.4 H_2O -aCCF

The H_2O emission's climate impact largely depends on its residence time. The likelihood of removing (rain-out) the emitted H_2O decreases with altitude up to the tropopause. Or vice versa, the H_2O emission's residence time increases with the height and shows a sharp gradient at the tropopause (Grewe and Stenke, 2008; Wilcox et al., 2012). Hence the distance to the tropopause is already a good indicator of the H_2O 's lifetime. There are different tropopause definitions, for instance, temperature lapse rate (including the World Meteorological Organization (WMO), thermal tropopause (WMO, 1957)) and

265

potential vorticity (PV) (Kunz et al., 2011). The WMO thermal tropopause and the PV dynamical tropopause may differ locally (Grewe and Dameris, 1996). van Manen and Grewe (2019) showed that PV is a better indicator for the H₂O-aCCF, since PV can also be used as a definition between tropospheric and stratospheric air masses.

270 The H₂O-aCCF in K/kg(fuel) is based on PV in the standard potential vorticity unit (PVU). For an atmospheric location (x, y, z) at time t with $PV = PV(x, y, z, t)$, the H₂O-aCCF can be found in Eq. (5).

$$aCCF_{H_2O}(PV) = 2.11 \times 10^{-16} + 7.70 \times 10^{-17} \times |PV|$$

$$aCCF_{H_2O} \approx P-ATR20_{H_2O}$$
(5)

Figure 5 shows an example of the H₂O aCCF in K/kg(fuel) on December 18th 2015 over Europe at 250 hPa. One can notice that the H₂O has warming effects in general, and the highest values occur at the location where the potential vorticity is also high (see Figure 3 b)).

275

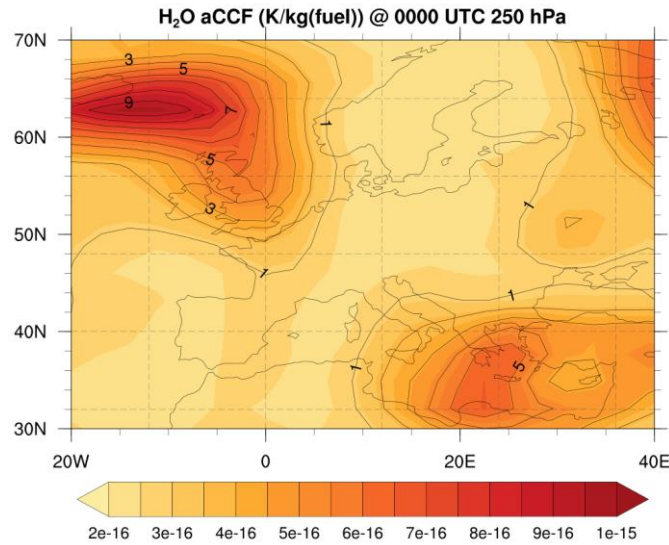


Figure 5 H₂O aCCF (colored contour) in K/kg(fuel) and potential vorticity (black contour) in standard potential vorticity unit (PVU) on December 18th 2015, at 250 hPa.

280 3.3.5 Contrail cirrus aCCF

Contrail cirrus is short-lived. Because of its contrasting effects on shortwave and longwave radiation, contrail cirrus's radiative and climate effects distinguish between day- and night-time. Thus, the specific radiative forcing of contrail cirrus in W/m² per flight distance has been developed for the day- and night-time conditions by E. Irvine (now Klingaman) based on reanalysis data (Klingaman and Shine, supplement). Note that, in the supplement, the contrail coverage is assumed to be either 1 or 0, which is reasonable for higher horizontal resolutions. Therefore contrail distance equals flight distance in a grid box. Here, however, we deal with lower horizontal resolutions of T42 (Section 3.1), and the conversion of flight distance to contrail distance requires the multiplication of the potential contrail coverage value of the regarded grid box. This approach ensures

285

290 that Grewe et al. (2014a) and the supplement are consistent. Unlike the other aCCFs formulas in calculating the P-ATR20 value directly, the algorithm of contrail cirrus estimates the global and annual mean specific RF per flight distance using the parametric equation of Schumann et al. (2012). Accordingly, the contrail-cirrus aCCF (an approximation of ATR20) for pulse emissions (P-ATR20_{contrail}) is obtained as a product of the specific RF per flight distance value and a constant of 0.0151 K/W/m² derived using AirClim model.

Night-time contrails aCCF

295 Night-time contrails refer to contrails with their entire (6 hours in this paper) lifetime occurring at night. Since these contrails exist only during hours of darkness, they cause only longwave RF, so their net RF must be positive (warming). The scatterplot of relevant meteorological variables against the net RF of night contrails was used to identify which parameters had the strongest relationships with the net RF (see Klingaman and Shine supplement). It was found that the local temperature can provide reasonable approximations for the night contrails' radiative effects. By using the nonlinear regression method, the specific RF per flight distance of night-time contrails (RF_{contrails-night}) in W/m²/km is derived based on temperature (T) in K.

300 For an atmospheric location (x, y, z) at time t, with T = T(x, y, z, t), the specific RF per flight distance of night-time contrail-cirrus can be found in Eq. (6). Please note that correlation is not valid for temperatures less than 201_K. For temperatures below 201_K, the value should be set to 0.

$$RF_{contrails-night} = \begin{cases} 10^{-10} \times (0.0073 \times 10^{0.0107 \times T} - 1.03) & \text{for } T > 201K \\ 0 & \text{else} \end{cases} \quad (6)$$

305 By multiplying the factor of 0.0151 K/W/m², the night-time contrails aCCF in K per flown-km is calculated in Eq. (7). As explained in section 2, the conversion factor from specific RF to ATR20 for contrails is obtained using the climate response model, AirClim (Grewe and Stenke, 2008; Dahlmann et al., 2016). We apply a consistent set of global emission inventory for a given scenario, for which the specific RF and ATR20 are calculated. The ratio between specific RF and ATR20 is then derived as 0.0151 K/W/m², hence used here as a conversion factor.

$$\begin{aligned} aCCF_{contrails-night} &= RF_{contrails-night} \times 0.0151 \\ aCCF_{contrails-night} &\approx P-ATR20_{contrails-night} \end{aligned} \quad (7)$$

310 *Day-time contrails aCCF*

Day-time contrails refer to contrails that form and dissipate during daylight or have a part of their 6-hour lifetime during the day. The specific RF per flight distance of day-time contrails (RF_{contrails-day}) in W/m²/km is based on the OLR in W/m² at the top of the atmosphere at the time and location of the contrail formation. Therefore, for an atmospheric location (x, y) at time t with OLR(x, y, t), the RF of day-time contrail-cirrus can be found in Eq. (8). Please note that Eq. (8) will predict negative specific -RF per flight distance for OLR < -193 W/m² and positive specific RF per flight distance for any larger OLR values.

315

$$RF_{contrails-day} = 10^{-10} \times (-1.7 - 0.0088 \times OLR) \quad (8)$$

Similarly, the day-time contrails aCCF in K_per flown-km is calculated in Eq. (9).

$$aCCF_{contrails-day} = RF_{contrails-day} \times 0.0151 \quad (9)$$

$$aCCF_{contrails-day} \approx P-ATR20_{contrails-day}$$

Please note that in the ACCF submodel, the contrail aCCF is only activated when the potential contrail coverage is larger than zero and the flight distance is converted to contrail distance by multiplying with the potential contrail coverage (see also above).

Depending on the time of the contrail-cirrus occurring, either day- or night-contrail-cirrus aCCF calculation is used.

Figure 6 shows an example of the day- and night-time contrail aCCF on December 18th 2015 over Europe at 250 hPa: a) 1200 UTC and b) 0000 UTC. One can see that the contrail aCCF depends on the formation time. For instance, at the exact location (e.g., over Ireland), contrail formed at 1200 UTC has a cooling effect, whereas at 0000 UTC has a warming impact.

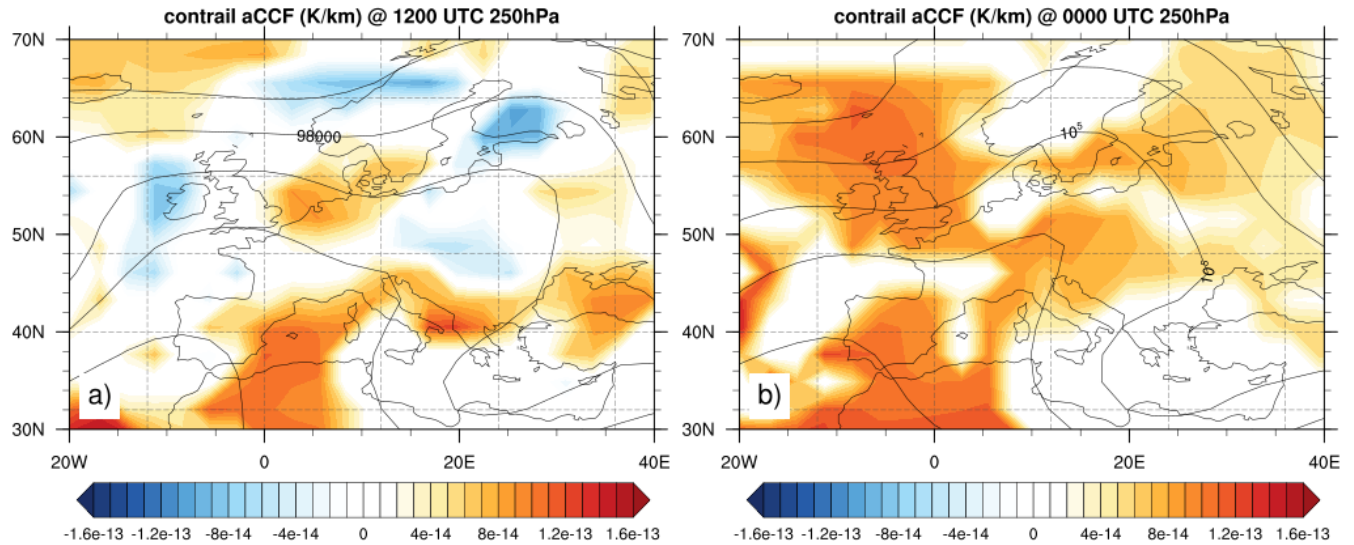


Figure 6 Contrail-cirrus aCCFs (colored contour) in K/km and geopotential height (black contour) in m^2/s^2 on December 18th 2015 at 250 hPa: a) 1200 UTC; b) 0000 UTC.

3.4 Physical climate metric and efficacy applied in the ACCF submodel

The aCCFs formulas provided in section 3.3 calculate the climate impact of O_3 , CH_4 , PMO, H_2O , and contrail-cirrus consistently in P-ATR20, i.e., for a pulse emission. With pulse emission, one could compare, for instance, the future impact of emissions in a given year. When a non-pulse emission is considered, e.g., an increased emission scenario representing the growth of air traffic, the metrics of pulse emission can be converted (Fuglestedt et al., 2010).

Here we demonstrate an example of converting the P-ATR20 to the ATR20 of the future BAU emission scenario (F-ATR20) derived by Grewe et al. (2021). We determined the climate metrics conversion factors for the aCCFs of O_3 , CH_4 , PMO, H_2O , and contrail cirrus using the AirClim model. We performed two simulations with pulse emissions in 2017 and future emission scenario BAU, respectively. For both simulations, we calculate the factor between ATR20 and RF for each effect and use the

ratio between these values as conversion factors. Table 1 shows the conversion factors from the P-ATR20 to the F-ATR20 metric. In the namelist of the ACCF 1.0, these metric conversion factors can be changed depending on the chosen scenario for different purposes (see supplement).

340 The efficacy of the individual forcing agents (O_3 , CH_4 , PMO, H_2O , and contrail-cirrus), which consider the different effects of these forcing agents in producing global temperature change (e.g., Hansen et al., 2005), are not included in the aCCF formulas in section 3.3. However, they can be easily included via namelist settings of the ACCF submodel (see the user manual in the supplement for namelist settings). The present study implemented the forcing efficacies in Lee et al. (2021), as shown in Table 1. The final output of the ACCF submodel is a product of the output of aCCFs formulas in section 3.3, the metric conversion factor, and the efficacies.

Table 1 Example values of climate metrics conversion factors from ATR20 of a pulse emission in 2017 (P-ATR20) to ATR20 of future BAU emission scenario (F-ATR20) and efficacies of different species/contrail-cirrus effect. The efficacies are taken from Lee et al. (2021).

Descriptions	Metric conversion factors (P-ATR20 → F-ATR20)	Efficacy
CO_2	9.4	1.0
NO_x-O_3	14.5	1.37
NO_x-CH_4	10.8	1.18
NO_x-CH_4-PMO	10.8	1.18
H_2O	14.5	1.0
Contrail-cirrus	13.6	0.42

4 ACCF model simulations

350 In this section, we present the application of the submodel ACCF, how it describes the climate effects of aviation emissions and how it can be used for aircraft trajectory optimisation. This section also presents the quality check of ACCF submodel outputs. Firstly, we compare the climatology of the prototype aCCFs for O_3 , CH_4 , H_2O , and contrail-cirrus to results from the literature. Secondly, we study the O_3 RF change caused by the air traffic emissions through the AirTraf submodel calculated online for cost- and climate- optimal flights, respectively. The climate-optimized flights minimized the NO_x -induced O_3 effect computed using Eq. (1).

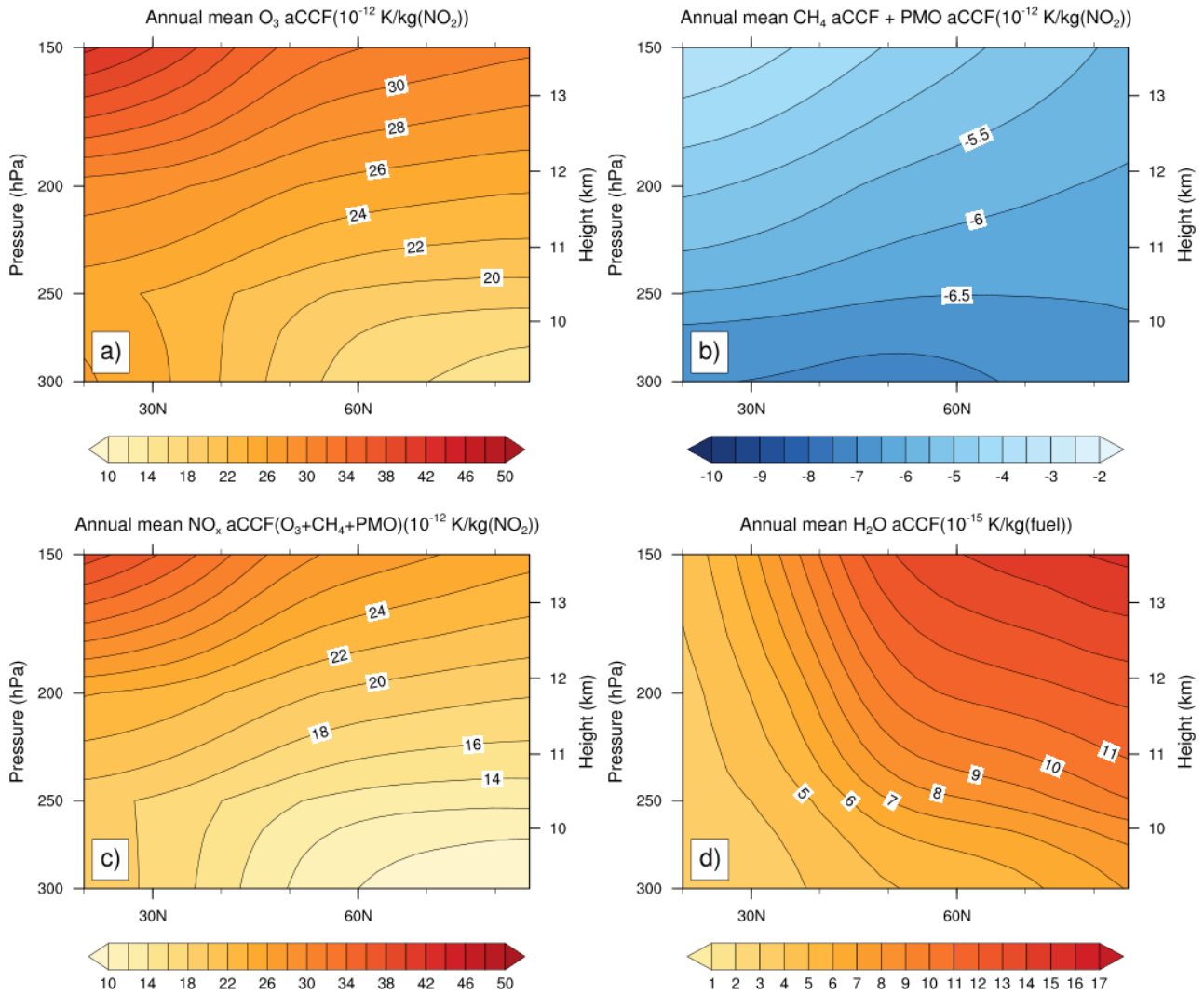
4.1 Climatology of aCCFs

360 The climatological aCCFs are calculated for all meteorological situations emerging over a one-year nudged simulation in 2016. The climate metric conversion factors and the efficacies in Table 1 are considered. Figure 7 a)-c) shows the annual and zonal mean aCCF from O_3 , CH_4 combined with PMO, and total NO_x (O_3+CH_4+PMO), respectively. The considered region is over the northern hemisphere and between 150-300 hPa.

The warming effects of O₃ increase with the altitude and towards the lower latitudes, which is in line with other studies. For instance, Fig A.2 of Dahlmann et al. (2016) shows that the global annual mean RF of aviation NO_x-induced O₃ increases with the pressure altitude. Figure 8 of Grewe and Stenke (2008) shows the global mean temperature change of NO_x-induced O₃ for 2100, considering a constant emission from 2050-2100. Due to different emission scenarios, the absolute value in Fig. 7 of
365 this study is much lower (order of magnitudes). However, when comparing the vertical and lateral variability in the vertical range of 150 and 300 hPa (typical flight corridor range), a similar pattern can be observed.

In comparison, the cooling effect of CH₄ (including PMO) increases towards lower altitudes but shows less dependency on latitude than O₃ at the lower altitude. That is to say, if the flight altitude is reduced, one would expect more substantial cooling effects due to NO_x-induced CH₄ depletion. Such phenomena are in line with the study of Frömming et al. (2012), where it was
370 shown that the CH₄ mean RF reduces when flying lower. Furthermore, when comparing Fig. 8 of Grewe and Stenke (2008) and Fig. A.2 of Dahlmann et al. (2016) in the same vertical range, we notice some discrepancies in the CH₄ aCCF pattern in the latitudinal directions. Both Fig. 8 and Fig. A.2 show that the cooling effects of CH₄ increase towards lower latitudes. This was also observed in Köhler et al. (2013). However, Fig. 7 b) shows an opposite trend, which needs further diagnosis in future studies. Since the value of CH₄ aCCF is about five times smaller than the O₃ aCCF, one can consider the mismatch of CH₄
375 aCCF to be of minor importance.

Figure 7 d) shows the annual zonal mean H₂O aCCF. The warming effects of H₂O increase with altitude and towards the polar region, which matches well with the previous study of Grewe and Stenke (2008), confirming that ACCF accurately represents the variations in global climate change of aviation H₂O emissions at the different regional locations and different altitudes.



380 **Figure 7 Annual zonal mean aCCFs (F-ATR20) in the northern hemisphere and the between 150 to 300 hPa**
attributed to a) NO_x-O₃ effects; b) NO_x-CH₄ (+PMO) effects; c) overall NO_x effects (O₃+CH₄+PMO); d) H₂O effects

Figure 8 shows the zonal mean climatological value of contrail cirrus aCCFs in K/km by combining the day and night effects. The RF and hence the F-ATR20 are calculated at the location where contrails could be formed. We compare the climatological contrail-cirrus aCCF with the values presented in the previous literature (Fig. A.2. of Dahlmann et al. (2016), where the annual zonal mean contrails RF per flown km are calculated using normalized emissions). We notice that the order of magnitude and the profile of the contrail aCCF matches the study of Dahlmann et al. (2016).

385

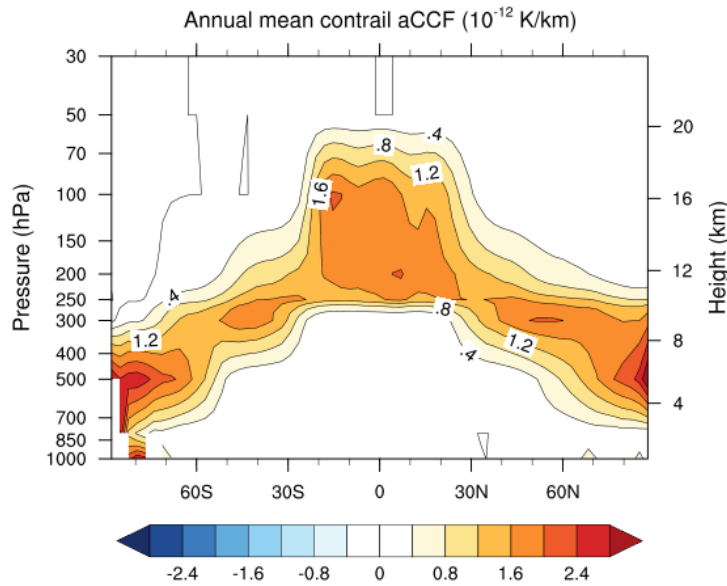


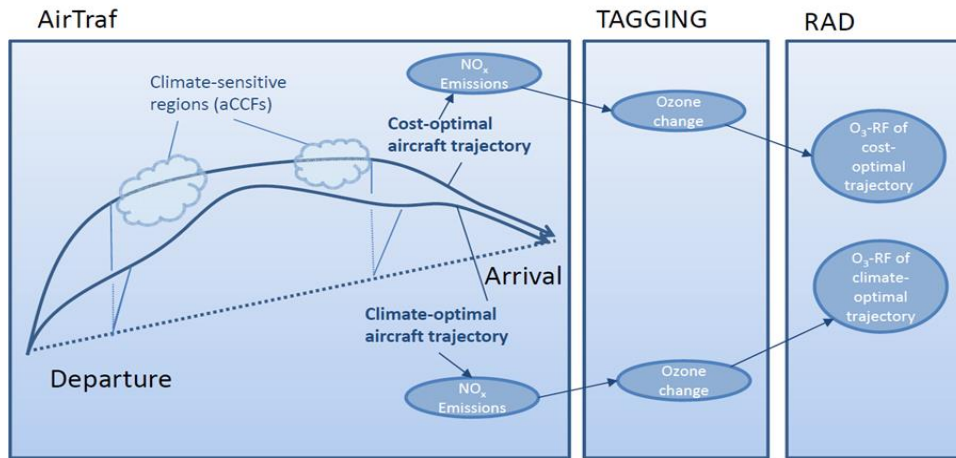
Figure 8 Annual zonal mean contrail aCCF (F-ATR20) in K/km: combined effects of day and night contrails.

390 **4.2 Radiative forcing calculation of aircraft emissions using EMAC submodels**

To demonstrate the usage of the ACCF 1.0 in aircraft trajectory optimisation considering non-CO₂ climate effects, we use the O₃ aCCF to calculate the RF due to aviation NO_x-induced O₃ by combining ACCF with AirTraf, TAGGING, and RAD (EMAC submodels). Figure 9 shows how an aircraft trajectory from the departure to the arrival airport is guided through climate-sensitive regions, described with the help of the ACCF submodel. Providing atmospheric perturbations in reactive species to the TAGGING submodel calculates associated ozone changes, and eventually, radiative impacts are characterized in the RAD submodel. For the demonstration, we optimize the flight trajectories of a subset of daily European flights concerning either minimum cost (simple operating cost option in the AirTraf submodel (Yamashita et al., 2020)) or minimum climate impact from only NO_x-induced O₃ effect only. In two different simulations, the associated NO_x emissions alter O₃ concentrations and thus their RF differently. The hypothesis of the reduced RF in climate-optimized routes would prove the concept of the O₃ aCCFs. For a more detailed study, the climate impact of aviation NO_x emissions should be a combination of O₃, CH₄, PMO, and SWV decrease. Here we focus on the short-term O₃ effect to better understand the particular feature of the O₃ aCCF.

395

400



405

Figure 9 Sketch of the radiative forcing calculations for ozone changes caused by online air traffic NO_x emissions for cost- and climate-optimized flight trajectories. Cost-optimal aircraft trajectories minimize the simple operating cost of the flight, while, climate-optimal aircraft trajectories minimize the climate impact (here only the NO_x-induced O₃ effect is included).

410

In line with the simulation scheme above, we configured the EMAC model with a list of EMAC submodels. In addition to the standard submodels, we use AirTraf 2.0 (Yamashita et al., 2020) to calculate the air traffic emissions from different flight trajectories, MECCA (Module Efficiently Calculating the Chemistry of the Atmosphere, Sander et al., 2005) and SCAV (SCAVenging, Tost et al., 2006a) to represent the chemical kinetics of EMAC. We also use TAGGING 1.0 (Grewe et al., 2017a) to tag the contributions of emissions to concentrations. The radiation flux change of the NO_x-induced O₃ change is calculated using the submodel RAD (Dietmüller et al., 2016). The complete list of used EMAC submodels in this simulation can be found in Table A.1 of the Appendix.

415

The simulation setup for trajectory optimization is given in Table 2. 85 daily European flights are used. The constant flight Mach number 0.82 combined with the wind speed will result in different ground speeds. **For cost-optimized flight trajectories, simple operating cost calculated using Eq. (10) is the objective function. For climate-optimized flight trajectories, the F-ATR20 of NO_x-induced O₃ is used as the objective function. There are 11 design variables to express a flight trajectory. Five variables control the vertical change between flight levels of 29000 ft (FL290) and 41000 ft (FL410), and six variables control the lateral shift.** The Adaptive Range Multi-objective Genetic Algorithm (ARMOGA version 1.2.0, (Sasaki and Obayashi, 2005; Sasaki et al., 2002)) is implemented for trajectory optimization.

420

$$\text{cost} = C_t \cdot t + C_f \cdot m_{\text{fuel}} \quad (10)$$

where t is the flight time in hrs, m_{fuel} is the fuel consumption in kg, C_t is the flight time related cost in €/hr; and C_f is the fuel related cost in €/kg (fuel).

425

Table 2 AirTraf simulation setup for trajectory optimizations considering cost minimum and climate minimum (only NO_x-O₃ effect), respectively.

Description		
AirTraf option	Cost-optimized	Climate-optimized
ECHAM5 Resolution	T42/L31ECMWF (2.8°× 2.8° in latitude and longitude, 31 vertical pressure levels up to 10 hPa, a time step of 12 minutes)	
Flight plan	85 daily European flights	
Aircraft / Engine type	A330/CF6 engine model	
Flight altitude in feet	[FL290, FL410]	
Optimization objective	Minimum simple operating cost	Minimum F-ATR20 of NO _x -O ₃

Figure 10 shows the calculated flight trajectories on a single day for the minimal cost (red) and the minimal NO_x-O₃ climate impact (green). Figure 10 a) shows the changes in flight altitudes, and Figure 10 b) shows the lateral shifts of flight trajectories aggregated along the vertical direction. For cost-optimized flights, the aircraft tends to fly as high as possible within the vertical constraints to maximize aerodynamic efficiency, reducing fuel consumption and the associated operational cost. As for the climate-optimized routine, the situation is much more complicated. The climate impact of O₃ attributed to NO_x emissions depends on multi-criteria, e.g., the emitted quantity, time, location, and weather. On average, the altitudes of climate-optimized flights are lower than those of cost-optimized flights. We also notice from Figure 10 b) that some flights tend to shift northward to reduce the NO_x-O₃ climate impact.

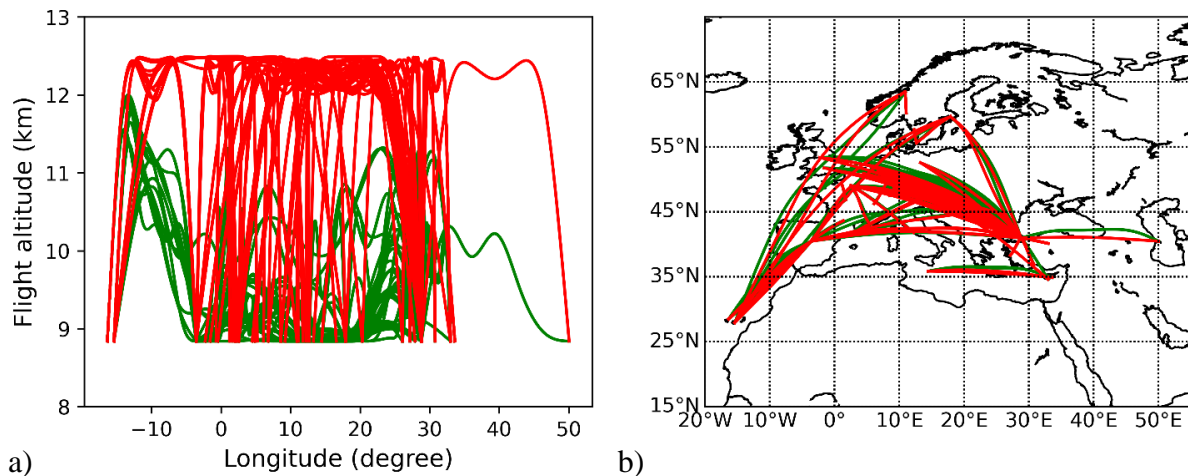


Figure 10 Calculated daily flight trajectories in a) vertical variation and b) lateral variation using AirTraf for cost-optimized (red) and climate optimal considering only the NO_x-O₃ effects (green).

The flight characteristics and performance data are summarized in Table 3. Compared to the cost-optimized flights, the fuel consumption of the climate-optimized flights is 11% higher, and the NO_x emissions are 15% higher. The total cost of climate-optimized flights is about 5% higher than that of cost-optimized flights.

Table 3 Daily sum over the flight-plan of the characteristics of the cost-optimized and the NO_x-O₃-optimized flights.

Parameters	Cost-optimized	NO _x -O ₃ -optimized	Diff %
Fuel consumption [Tons]	728	810	+11
NO _x emissions [Tons]	7.26	8.33	+15
Flight time [hrs]	157	156	-0.6
Flight distance [km]	134000	134346	+0.3
Cost [thousand EUROS]	636.56	667.76	+4.9

Having the flight trajectories and their respective performance calculated with AirTraf using ACCF values (Figure 10), NO_x emissions from cost- and climate-optimal trajectories are then integrated into the global EMAC model as tagged species by the EMAC/TAGGING submodel. This allows for identifying the contributions of different NO_x emission sources to the atmospheric changes of the NO_x and O₃ concentrations. This showcase simulation using tagging chemistry was run for three months, from January to March 2016. Figure 11 shows relative changes in monthly mean mixing ratio distribution of a) NO_x in mol/mol and b) O₃ in mol/mol, comparing effects caused by NO_x emissions from climate-optimized flight trajectories with the effect of cost-optimized trajectories (baseline) in March 2016. The figure is presented in the vertical cross-section. The climate-optimized trajectories emit NO_x at a lower altitude than the cost-optimized trajectories; therefore, we see an increase in the NO_x mixing ratio at the lower altitude (indicated by the red color in Figure 11 a)). As a result, the O₃ production is shifted downwards (see Figure 11 b)). The residence time of O₃ at the lower altitude is shorter due to a more efficient wash-out. Therefore, the calculated RF of the NO_x induced O₃ for the climate-optimized flights (13.3 mW/m²) is about 2% less than that of the cost-optimized flights, which confirms that the climate-optimized flight trajectories based on the O₃ aCCF reduce the associated NO_x-O₃ climate effect.

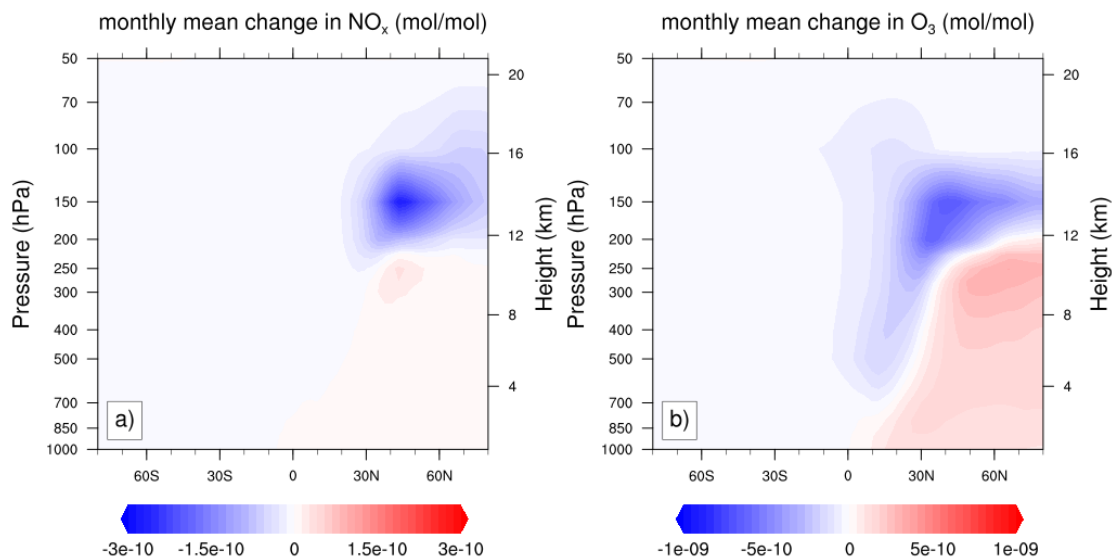


Figure 11 Changes of a) NO_x mixing ratio and b) resulting changes in O₃ mixing ratio caused by NO_x-O₃-optimized flight trajectories using only O₃ aCCF. The baseline is cost-optimized flights.

5 Application of the ACCF submodel for trajectory optimization

460 This section demonstrates the application of the ACCF submodel to assess the aviation climate effects during trajectory optimization. In the previous research, Yamashita et al. (2020) implemented the ACCF submodel in AirTraf 2.0 to obtain climate-optimized trajectories. Here, we update the ACCF submodel outputs using the physical climate metric F-ATR20 and consider the efficacy of radiative effects.

5.1 Simulation setup

465 We couple the ACCF 1.0 with the AirTraf 2.0 in this simulation. In AirTraf 2.0, two optimization objectives are considered, respectively: cost- and climate-optimized. The simulation setup can be seen in Table 4. In this section, the climate-optimized trajectory minimizes the total F-ATR20 of CO₂, NO_x (summation of O₃, CH₄, and PMO), H₂O, and day/night contrail-cirrus, including the efficacies of individual species/contrail-cirrus as shown in Table 1.

Table 4 AirTraf simulation setup for trajectory optimizations considering cost minimum and climate minimum.

Description		
AirTraf option	Cost-optimized	Climate-optimized
ECHAM5 Resolution	T42/L31ECMWF (2.8°×2.8° in latitude and longitude, 31 vertical pressure levels up to 10 hPa, a time step of 12 minutes)	
Flight plan	85 daily European flights	
Aircraft / Engine type	A320/CFM56 engine model	
Flight altitude in feet	[FL290, FL410]	
Optimization objective	Minimum simple operating cost	Minimum F-ATR20

470 5.2 Optimized flight trajectories

We compare the F-ATR20 values of cost-optimized (red) and climate-optimized (green) trajectories in Figure 12. Cost-optimized trajectories are characterized by higher flight altitudes to maximize aerodynamic efficiency, which is similar to what was described in section 4.2. On the other hand, climate-optimized trajectories considering non-CO₂ effects fly at lower altitudes at most locations to reduce the impact of the total NO_x, H₂O, and contrails.

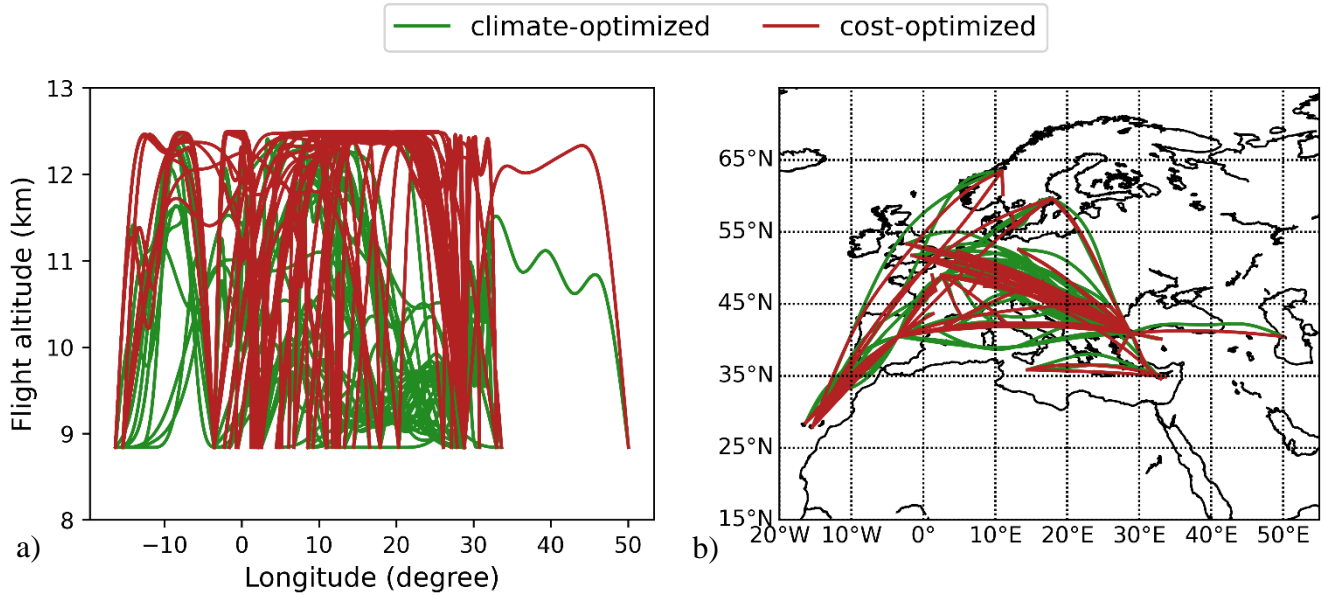
475 Table 5 summarizes the flight characteristics. Compared to the cost-optimized flights, the climate-optimized trajectories (ignoring economic costs while only minimizing climate effects) tend to increase fuel consumption by 17% and NO_x emissions by 25%. On the other hand, the total F-ATR20 is reduced by 51% driven by the contrails effect (-89%), followed by the combined CH₄ and PMO impact (-41%). The impact of CO₂ and H₂O is characterized by lower orders of magnitudes than the impacts from NO_x emissions and contrails; therefore, they are not crucial properties during the optimization process, but they
480 are affected by changes due to higher fuel consumption (causing higher CO₂ impact (+17%)) and lower mean flight altitudes (leading to lower H₂O impact (-33%)).

Furthermore, one can observe that the contribution of CO₂ to the overall climate impact is relatively low compared to the non-CO₂ effects. This could be caused by choice of the physical climate metric and the radiation scheme used to develop the

485 original CCFs and the following aCCFs characteristics. While ongoing research investigates how to best define an adequate climate metric reflecting short-term and long-term effects to a certain extent, we expect to develop a better understanding with further diagnosis.

Table 5 Daily sum of flight characteristics over the cost-optimized and the climate-optimized trajectories on December 18th 2015.

Parameters	Cost-optimized	Climate-optimized	Diff %
Fuel consumption [Tons]	337.5	394.9	+17.0
NO _x emissions [Tons]	3.600	4.497	+24.9
Flight time [hrs]	157.2	159.4	+1.3
Flight distance [km]	133862	137392	+2.6
Contrail distance [km]	41032.2	30074.1	-26.7
Cost [thousand EUROS]	596.9	632.1	+5.9
F-ATR20 CO ₂ [K]	2.373e-09	2.777e-09	+17.0
F-ATR20 H ₂ O [K]	2.861e-09	1.910e-09	-33.2
F-ATR20 NO _x - O ₃ [K]	1.050e-07	9.852e-08	-6.2
F-ATR20 NO _x - CH ₄ +PMO [K]	-2.058e-08	-2.907e-08	-41.3
F-ATR20 contrails [K]	7.209e-08	7.644e-09	-89.4
F-ATR20 total [K]	1.618e-07	7.908e-08	-51.1



490 **Figure 12 Comparison of a) vertical shift and b) lateral shift between cost-optimized (red) and climate-optimized (green) trajectories on December 18th 2015.**

6 Discussions

This research implements a consistent set of prototype algorithmic climate change functions as the submodel ACCF 1.0 of EMAC, enabling quantifying aviation emission climate effects. The demonstration simulations confirm that the developed

495 aCCFs can predict the characteristic patterns of ATR20 from H₂O, NO_x-induced O₃, and contrail-cirrus. The NO_x-induced CH₄ pattern shows a slight discrepancy in terms of latitudinal variabilities when compared to previous studies (Grewe and Stenke, 2008, Frömming et al., 2012, Köhler et al., 2013). As the total NO_x aCCF is dominated by the positive O₃, we expect that the combination of O₃ and CH₄ captures the feature of aviation NO_x adequately. Further development of the CH₄ aCCF formula is required to address the latitudinal discrepancy.

500 Furthermore, the ACCF submodel has been implemented in a comprehensive tagging chemistry simulation chain to evaluate mitigation gains because of modified aviation emissions. By coupling the ACCF submodel with the AirTraf submodel, NO_x emissions are calculated from cost-optimized and climate-optimized flights considering only the NO_x induced O₃ effect. The NO_x emissions are then fed into the tagging chemistry scheme to estimate the resulting RF due to changes in O₃ mixing ratios. The results confirmed that the climate-optimized trajectories reduce the RF of O₃ by 2% compared to the cost-optimized flights.

505 The case study on trajectory optimization for cost- and climate-optimized flights indicates a relatively low contribution of CO₂ to the overall climate impact compared to the non-CO₂ effects. Our first thoughts are that this might be related to the metrics we are using, the radiation scheme in developing the original CCFs models, and the regional effects. Ongoing work in the metric diagnosis and the geographical analysis will help us better understand the reasons.

Nevertheless, the aCCFs 1.0 used in this study represent a prototype formulation and face different aspects of uncertainties.

510 The aCCFs are based on simulations performed for the North Atlantic Flight Corridor during summer and winter. Using them at other locations and seasons should be done cautiously and carefully evaluated. Additionally, physical climate metrics can be defined on time horizons, e.g., 20, 50, and 100 years. We would like to note here that the development of the aCCFs is an ongoing research activity and an expansion of their geographic scope and seasonal representativeness is under investigation.

6.1 Climate metrics conversion

515 Regarding the physical climate metric used in this study, the aCCFs formulas in section 3 calculate the average temperature response over 20 years for a pulse emission (P-ATR20). Based on the P-ATR20, it is possible to obtain different physical climate metrics for any other emission scenario by applying a climate response model, e.g., AirClim. Though the flexibility of the ACCF namelist setup allows the user to convert the climate metrics, the metric selection involves different factors, e.g., the perspective question (Fuglestvedt et al., 2010; Grewe and Dahlmann, 2015). We want to stress that we consider it essential

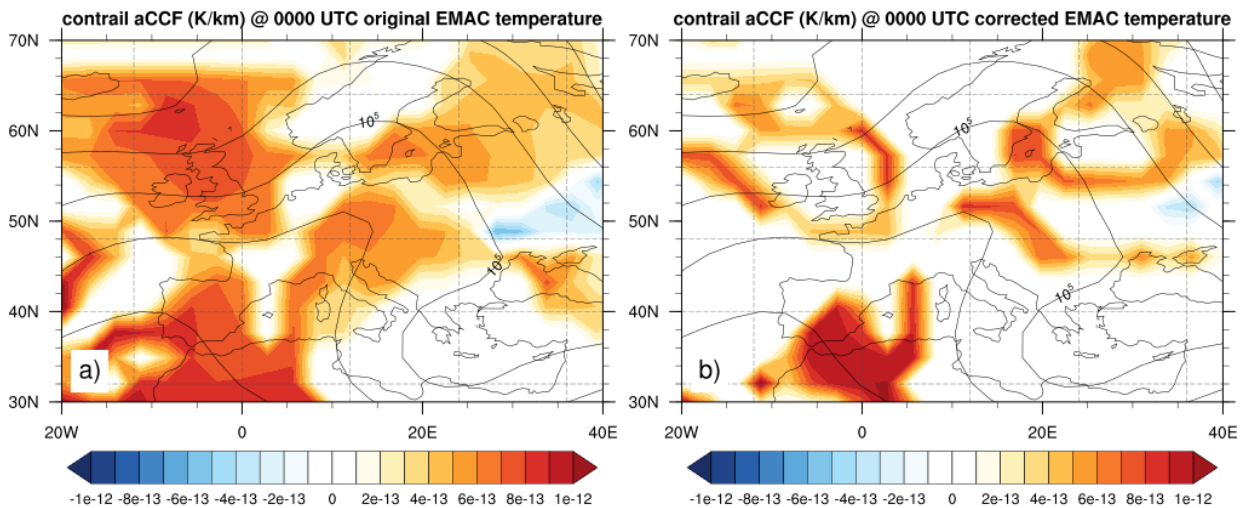
520 that any optimization study carefully defines the physical climate metric used, the type of strategic decision envisaged, constraints given, and assumptions on policy and regulations accepted. For instance, one should identify the application scenario (or the perspective question) as the specific application scenario is critical for defining the adequate reference, the physical climate metric, and the emission scenario. A pulse emission would compare the future climate impact in a given year. A future emission scenario would compare the effect of varying emissions over a period in the future. From the perspective

525 question, an adequate climate indicator and time horizon can then be deduced.

6.2 Uncertainties of contrail aCCFs

The contrail aCCFs face different sources of uncertainties. Here we discuss two aspects: the sensitivity to the meteorological input and the uncertainties in the scientific understanding of climate science which is moderate or low (see, e.g., Lee et al., 2021).

530 The characteristics of aCCFs are sensitive to the input of meteorological conditions. For instance, the potcov varies strongly with the local atmospheric temperature and relative humidity over ice, which again has a dependency on the specific models (e.g., an Earth system climate model vs. a weather forecast model with higher resolution). While comparing the temperature field calculated from the EMAC model on December 18th 2015 nudged towards the ECMWF reanalysis data (ERA-Interim) with the original ERA-Interim datasets at three pressure levels of 200 hPa, 250 hPa, and 300 hPa, we observed that the
535 temperature calculated from the EMAC model is on average 3 K lower than the reanalysis data. This temperature difference affects the predicted potcov and the calculated contrail-cirrus aCCF (see Eq. (6)). Figure 13 shows a comparison between the values of F-ATR20 calculated from contrail-cirrus aCCF on December 18th 2015 at 250 hPa. Figure 13 (a) shows the geographical pattern using the original EMAC temperature, and Figure 13 (b) shows the geographical pattern when artificially correcting the 3 K temperature bias from the EMAC temperature. Two effects are observed: 1) the areas where the contrails might form are reduced for a warmer temperature; 2) the maximum value of ATR20 increases indicating a more substantial
540 warming effect. From this preliminary analysis, we could see that the uncertainties related to the inputs of aCCFs play an essential role in the robustness of the aCCFs results.



545 **Figure 13 Geographical distribution of contrail aCCF in K/km on 18th December 2015 at 250 hPa for a) the original EMAC temperature and b) the bias-corrected EMAC temperature.**

6.3 Ongoing research on the robustness of aCCFs

While the non-CO₂ effects, especially the aviation-induced contrail-cirrus effects, play essential roles in aviation's climate impact, the related uncertainties still need to be resolved. The uncertainties of contrail-cirrus climate impact are subject to

different aspects, including the natural variability of the atmosphere and modelling uncertainties. Both uncertainties propagate
550 to contrail-cirrus aCCF. The comprehensive numerical simulations of CCFs were established for weather situations in the
North Atlantic Flight Corridor covering the airspace between Europe and the USA. The climatological pattern in vertical and
latitudinal variability matches other studies (Dahlmann et al., 2016). For trajectory optimization, it is essential to understand
how these CCFs deviate in different geographical regions and what that means for climate-optimized flights.

The prototype aCCFs 1.0 still experiences uncertainties in the quantitative estimates of weather forecast and climate impact
555 prediction. A concept toward robust aCCFs is under development, which will additionally integrate information about
uncertainties arising from low-level understanding of climate science (Matthes et al., 2022, in preparation). This robust aCCFs
will rely on a set of aCCFs that consider educated guess estimates of individual climate impacts. The basis of this educated
guess can be, e.g., the conservative estimates of the individual RF (see Lee et al. 2021). Additionally, the second set of aCCFs
560 will be provided to perform individual risk analyses originating from different sources of uncertainty. This will be done by
quantitatively estimating the error if a lower or higher climate impact is assumed. With that, we add up to low or high range
aCCFs estimates, respectively. This concept of robust aCCFs can be applied in aircraft trajectory optimization studies with
EMAC/AirTraf. The corresponding experiment design would rely on one reference optimization using the educated guess
aCCFs and sensitivity optimization experiments using the low- or high-range aCCFs estimates. A robust trajectory would be
565 characterized by not losing overall benefits (mitigation gains) even if lower or upper estimates of aCCFs are applied.
Technically, this could be solved by calling the ACCF submodel several times within the same simulation, using the range of
different aCCFs estimates.

7 Conclusions

We developed the submodel ACCF 1.0 of the chemistry-climate model EMAC to estimate the climate impact of aviation
emissions in the flight corridor of the northern hemisphere representing an implementation of aCCFs 1.0 formulas. The
570 submodel ACCF 1.0 was developed according to the MESSy standard and was thoroughly presented in this paper. This
submodel calculates aviation's climate impact of CO₂ emissions and non-CO₂ effects, such as from NO_x-induced O₃, NO_x-
induced CH₄ (including PMO), H₂O, and contrail-cirrus based on a consistent set of aCCFs. The mathematical formulation of
the individual prototype aCCFs 1.0 is provided.

The climatological profile of the NO_x-induced effect on ozone (O₃ aCCF) shows that the warming effects of NO_x-induced O₃
575 increase with the altitude between 150-300 hPa and towards lower latitudes. While the climatological distribution of H₂O
aCCF shows that the warming effect of H₂O increases towards higher altitudes or latitudes. By comparing to the literature, we
conclude that the vertical and latitudinal structure within the flight corridor of the northern hemisphere of the NO_x induced O₃
and H₂O are well represented by the aCCFs.

The NO_x-induced effect on methane (CH₄ aCCF) shows that cooling effects increase towards lower altitudes and higher
580 latitudes. Although the latitudinal variation of CH₄ aCCFs is less pronounced than for other species, it is somewhat of the

opposite tendency to the literature. Since the absolute value of CH₄ aCCF is mostly overcompensated by the O₃ aCCF, the total NO_x aCCF could still capture the vertical and latitudinal variability of the overall NO_x effects.

For the contrail-cirrus aCCF, the climatological pattern follows the potential contrail coverage. The calculated F-ATR20 value also matches the literature, except that contrail-cirrus aCCF generates values at low altitudes where contrails are not expected to be formed. This might be related to the threshold of temperature and humidity used for calculating the potential contrail coverage and the temperature bias in the EMAC model.

Using the tagging chemistry approach, we were able to show that climate-optimized trajectories based on O₃ aCCF indeed reduce the radiative forcing contribution from aviation NO_x induced O₃ compared to the cost-optimized trajectories.

Finally, the trajectory optimization results confirm that the total F-ATR20 of climate-optimized flights is about 51% lower than the cost-optimized flights, with the largest contribution from contrail-cirrus.

Code availability

ACCF 1.0 has been published for the first time as a submodel of the Modular Earth System Submodel System (MESSy) since version 2.53. MESSy is continuously further developed and applied by a consortium of institutions. The usage of MESSy and access to the source code are licensed to all affiliates of institutions members of the MESSy Consortium by signing the MESSy Memorandum of Understanding. More information can be found on the MESSy Consortium Website (<http://www.messy-interface.org>). The version presented here corresponds to ACCF 1.0. The status information for ACCF will be available on the website.

Supplement

The supplement related to this paper includes the development of contrail-cirrus aCCF and the user manual for the ACCF submodel setup.

Author contributions

FY and VG designed the submodel ACCF V1.0. FY implemented the coupling of ACCF V1.0 with the Modular Earth Submodel System (MESSy). VG, SM, KD, EK, and KS developed the algorithmic Climate Change Functions (aCCFs). KD calculated the metric conversion factor. CF calculated the Climate Change Functions (CCFs). HY and VG designed the submodel AirTraf V2.0. BL and FL provided the traffic sample for this study. PR, SD, SM, and PP contributed to the discussions. FY and FC performed the simulations and analysed the results presented in this paper.

Competing interests

The authors declare that they have no conflict of interest.

Acknowledgment

610 The current study has been supported by the previous ATM4E project and the current FlyATM4E project. Both projects have received funding from the SESAR Joint Undertaking under grant agreements No. 699395 (ATM4E) and No. 891317 (FlyATM4E) under European Union's Horizon 2020 research and innovation program. [The computing resources to conduct simulations with the ECHAM/MESSy Atmospheric Chemistry \(EMAC\) model were provided by the TU Delft High Performance Cluster \(HPC12\). This work used resources of the Deutsches Klimarechenzentrum \(DKRZ\) granted by its Scientific Steering Committee \(WLA\) under project ID bd0781 and bd1062.](#)

References

- Airbus (2018). Global Market Forecast: Global Networks, Global Citizens 2018-2037. (eds.]. Toulouse, France.
- Burkhardt, U. and Kärcher, B. (2011). "Global radiative forcing from contrail cirrus." *Nature Climate Change*, 1: 54. DOI: 10.1038/nclimate1068.
- 620 Chen, C. C. and Gettelman, A. (2016). "Simulated 2050 aviation radiative forcing from contrails and aerosols." *Atmospheric Chemistry and Physics*, 16(11): 7317-7333. DOI: 10.5194/acp-16-7317-2016.
- Dahlmann, K., Grewe, V., Frömming, C. and Burkhardt, U. (2016). "Can we reliably assess climate mitigation options for air traffic scenarios despite large uncertainties in atmospheric processes?" *Transportation Research Part D: Transport and Environment*, 46: 40-55. DOI: <https://doi.org/10.1016/j.trd.2016.03.006>.
- 625 Dee, D. P., Uppala, S. M., Simmons, A. J., Berrisford, P., Poli, P., Kobayashi, S., Andrae, U., Balmaseda, M. A., Balsamo, G., Bauer, P., Bechtold, P., Beljaars, A. C. M., van de Berg, L., Bidlot, J., Bormann, N., Delsol, C., Dragani, R., Fuentes, M., Geer, A. J., Haimberger, L., Healy, S. B., Hersbach, H., Hólm, E. V., Isaksen, I., Kållberg, P., Köhler, M., Matricardi, M., McNally, A. P., Monge-Sanz, B. M., Morcrette, J.-J., Park, B.-K., Peubey, C., de Rosnay, P., Tavolato, C., Thépaut, J.-N. and Vitart, F. (2011). "The ERA-Interim reanalysis: configuration and performance of the data assimilation system." *Quarterly Journal of the Royal Meteorological Society*, 137(656): 553-597. DOI: <https://doi.org/10.1002/qj.828>.
- 630 Dietmüller, S., Jöckel, P., Tost, H., Kunze, M., Gellhorn, C., Brinkop, S., Frömming, C., Ponater, M., Steil, B., Lauer, A. and Hendricks, J. (2016). "A new radiation infrastructure for the Modular Earth Submodel System (MESSy, based on version 2.51)." *Geoscientific Model Development*, 9(6): 2209-2222. DOI: 10.5194/gmd-9-2209-2016.
- Frömming, C., Grewe, V., Brinkop, S. and Jöckel, P. (2014). "Documentation of the EMAC submodels AIRTRAC 1.0 and CONTRAIL 1.0." supplementary material of Grewe et al., 2014a, *Geoscientific Model Development*, 7. DOI: <https://doi.org/10.5194/gmd-7-175-2014>.

- Frömming, C., Grewe, V., Brinkop, S., Jöckel, P., Haslerud, A. S., Rosanka, S., van Manen, J. and Matthes, S. (2021). "Influence of the actual weather situation on aviation climate effects: The REACT4C Climate Change Functions." *Atmospheric Chemistry and Physics*, 21: 9151-9172. DOI: <https://doi.org/10.5194/acp-21-9151-2021>.
- 640 Frömming, C., Ponater, M., Dahlmann, K., Grewe, V., Lee, D. S. and Sausen, R. (2012). "Aviation-induced radiative forcing and surface temperature change in dependency of the emission altitude." *Journal of Geophysical Research: Atmospheres*, 117(D19). DOI: <https://doi.org/10.1029/2012JD018204>.
- Fuglestad, J. S., Shine, K. P., Berntsen, T., Cook, J., Lee, D. S., Stenke, A., Skeie, R. B., Velders, G. J. M. and Waitz, I. A. (2010). "Transport impacts on atmosphere and climate: Metrics." *Atmospheric Environment*, 44(37): 4648-4677. DOI: <https://doi.org/10.1016/j.atmosenv.2009.04.044>.
- 645 <https://doi.org/10.1016/j.atmosenv.2009.04.044>.
- Gottelman, A., Chen, C. C. and Bardeen, C. G. (2021). "The climate impact of COVID-19-induced contrail changes." *Atmos. Chem. Phys.*, 21(12): 9405-9416. DOI: 10.5194/acp-21-9405-2021.
- Grewe, V. (2006). "The origin of ozone." *Atmospheric Chemistry and Physics*, 6(6): 1495-1511. DOI: 10.5194/acp-6-1495-2006.
- 650 Grewe, V., Champougny, T., Matthes, S., Frömming, C., Brinkop, S., Søvde, O. A., Irvine, E. A. and Halscheidt, L. (2014b). "Reduction of the air traffic's contribution to climate change: A REACT4C case study." *Atmospheric Environment*, 94: 616-625. DOI: <https://doi.org/10.1016/j.atmosenv.2014.05.059>.
- Grewe, V. and Dahlmann, K. (2015). "How ambiguous are climate metrics? And are we prepared to assess and compare the climate impact of new air traffic technologies?" *Atmospheric Environment*, 106: 373-374.
- 655 Grewe, V., Dahlmann, K., Flink, J., Frömming, C., Ghosh, R., Gierens, K., Heller, R., Hendricks, J., Jöckel, P., Kaufmann, S., Kölker, K., Linke, F., Luchkova, T., Lührs, B., Van Manen, J., Matthes, S., Minikin, A., Niklaß, M., Plohr, M., Righi, M., Rosanka, S., Schmitt, A., Schumann, U., Terekhov, I., Unterstrasser, S., Vázquez-Navarro, M., Voigt, C., Wicke, K., Yamashita, H., Zahn, A. and Ziereis, H. (2017c). "Mitigating the Climate Impact from Aviation: Achievements and Results of the DLR WeCare Project." *Aerospace*, 4(3): 34. DOI: <https://doi.org/10.3390/aerospace4030034>.
- 660 Grewe, V. and Dameris, M. (1996). "Calculating the global mass exchange between stratosphere and troposphere." *Annales Geophysicae*, 14(4): 431-442. DOI: 10.1007/s00585-996-0431-x.

- Grewe, V., Frömming, C., Matthes, S., Brinkop, S., Ponater, M., Dietmüller, S., Jöckel, P., Garny, H., Tsati, E. and Dahlmann, K. (2014a). "Aircraft routing with minimal climate impact: the REACT4C climate cost function modelling approach (V1. 0)." *Geoscientific Model Development*, 7(1): 175-201. DOI: <https://doi.org/10.5194/gmd-7-175-2014>.
- 665 Grewe, V., Gangoli Rao, A., Grönstedt, T., Xisto, C., Linke, F., Melkert, J., Middel, J., Ohlenforst, B., Blakey, S., Christie, S., Matthes, S. and Dahlmann, K. (2021). "Evaluating the climate impact of aviation emission scenarios towards the Paris agreement including COVID-19 effects." *Nature Communications*, 12(1): 3841. DOI: 10.1038/s41467-021-24091-y.
- Grewe, V., Matthes, S., Frömming, C., Brinkop, S., Jöckel, P., Gierens, K., Champougny, T., Fuglestedt, J., Haslerud, A., Irvine, E. and Shine, K. (2017b). "Feasibility of climate-optimized air traffic routing for trans-Atlantic flights." *Environmental*
670 *Research Letters*, 12(3): 034003. DOI: 10.1088/1748-9326/aa5ba0.
- Grewe, V. and Stenke, A. (2008). "AirClim: an efficient tool for climate evaluation of aircraft technology." *Atmospheric Chemistry and Physics*, 8(16): 4621-4639. DOI: 10.5194/acp-8-4621-2008.
- Grewe, V., Tsati, E. and Hoor, P. (2010). "On the attribution of contributions of atmospheric trace gases to emissions in atmospheric model applications." *Geoscientific Model Development*, 3(2): 487-499. DOI: 10.5194/gmd-3-487-2010.
- 675 Grewe, V., Tsati, E., Mertens, M., Frömming, C. and Jöckel, P. (2017a). "Contribution of emissions to concentrations: the TAGGING 1.0 submodel based on the Modular Earth Submodel System (MESSy 2.52)." *Geoscientific Model Development*, 10(7): 2615-2633. DOI: 10.5194/gmd-10-2615-2017.
- Hansen, J., Sato, M., Ruedy, R., Nazarenko, L., Lacis, A., Schmidt, G. A., Russell, G., Aleinov, I., Bauer, M., Bauer, S., Bell, N., Cairns, B., Canuto, V., Chandler, M., Cheng, Y., Del Genio, A., Faluvegi, G., Fleming, E., Friend, A., Hall, T., Jackman,
680 C., Kelley, M., Kiang, N., Koch, D., Lean, J., Lerner, J., Lo, K., Menon, S., Miller, R., Minnis, P., Novakov, T., Oinas, V., Perlwitz, J., Perlwitz, J., Rind, D., Romanou, A., Shindell, D., Stone, P., Sun, S., Tausnev, N., Thresher, D., Wielicki, B., Wong, T., Yao, M. and Zhang, S. (2005). "Efficacy of climate forcings." *Journal of Geophysical Research: Atmospheres*, 110(D18). DOI: <https://doi.org/10.1029/2005JD005776>.
- Heymsfield, A., Baumgardner, D., DeMott, P., Forster, P., Gierens, K. and Kärcher, B. (2010). "Contrail Microphysics." *Bulletin Of The American Meteorological Society*, 91(4): 465-472. DOI: 10.1175/2009bams2839.1.
685
- Irvine, E. A. (2017). ATM4E internal report: Contrail algorithmic Climate Change Function derivation. (eds.)].
- Irvine, E. A., Hoskins, B. J., Shine, K. P., Lunnon, R. W. and Froemming, C. (2013). "Characterizing North Atlantic weather patterns for climate-optimal aircraft routing." *Meteorological Applications*, 20(1): 80-93. DOI: 10.1002/met.1291.

- 690 Jöckel, P., Kerkweg, A., Pozzer, A., Sander, R., Tost, H., Riede, H., Baumgaertner, A., Gromov, S. and Kern, B. (2010). "Development cycle 2 of the Modular Earth Submodel System (MESSy2)." *Geoscientific Model Development*, 3(2): 717-752. DOI: 10.5194/gmd-3-717-2010.
- Jöckel, P., Tost, H., Pozzer, A., Brühl, C., Buchholz, J., Ganzeveld, L., Hoor, P., Kerkweg, A., Lawrence, M. G., Sander, R., Steil, B., Stiller, G., Tanarhte, M., Taraborrelli, D., van Aardenne, J. and Lelieveld, J. (2006). "The atmospheric chemistry general circulation model ECHAM5/MESSy1: consistent simulation of ozone from the surface to the mesosphere." *Atmospheric Chemistry and Physics*, 6(12): 5067-5104. DOI: 10.5194/acp-6-5067-2006.
- 695 Kärcher, B. (2018). "Formation and radiative forcing of contrail cirrus." *Nature Communications*, 9(1): 1824. DOI: 10.1038/s41467-018-04068-0.
- Kärcher, B., Möhler, O., DeMott, P. J., Pechtl, S. and Yu, F. (2007). "Insights into the role of soot aerosols in cirrus cloud formation." *Atmospheric Chemistry and Physics*, 7(16): 4203-4227. DOI: 10.5194/acp-7-4203-2007.
- 700 Kerkweg, A., Buchholz, J., Ganzeveld, L., Pozzer, A., Tost, H. and Jöckel, P. (2006a). "Technical Note: An implementation of the dry removal processes DRY DEPosition and SEDImentation in the Modular Earth Submodel System (MESSy)." *Atmospheric Chemistry and Physics*, 6(12): 4617-4632. DOI: 10.5194/acp-6-4617-2006.
- Kerkweg, A., Sander, R., Tost, H. and Jöckel, P. (2006b). "Technical Note: Implementation of prescribed (OFFLEM), calculated (ONLEM), and pseudo-emissions (TNUDGE) of chemical species in the Modular Earth Submodel System (MESSy)." *Atmospheric Chemistry and Physics*, 6: 3603-3609.
- 705 Köhler, M. O., Rädcl, G., Shine, K. P., Rogers, H. L. and Pyle, J. A. (2013). "Latitudinal variation of the effect of aviation NO_x emissions on atmospheric ozone and methane and related climate metrics." *Atmospheric Environment*, 64: 1-9. DOI: <https://doi.org/10.1016/j.atmosenv.2012.09.013>.
- Kunz, A., Konopka, P., Müller, R. and Pan, L. L. (2011). "Dynamic tropopause based on isentropic potential vorticity gradients." *Journal of Geophysical Research*, 116: D01110. DOI: 10.1029/2010jd014343.
- Lee, D. S., Fahey, D. W., Skowron, A., Allen, M. R., Burkhardt, U., Chen, Q., Doherty, S. J., Freeman, S., Forster, P. M., Fuglestedt, J., Gettelman, A., De León, R. R., Lim, L. L., Lund, M. T., Millar, R. J., Owen, B., Penner, J. E., Pitari, G., Prather, M. J., Sausen, R. and Wilcox, L. J. (2021). "The contribution of global aviation to anthropogenic climate forcing for 2000 to 2018." *Atmospheric Environment*: 117834. DOI: <https://doi.org/10.1016/j.atmosenv.2020.117834>.

- 715 Lund, M. T., Aamaas, B., Berntsen, T., Bock, L., Burkhardt, U., Fuglestedt, J. S. and Shine, K. P. (2017). "Emission metrics for quantifying regional climate impacts of aviation." *Earth Syst. Dynam.*, 8(3): 547-563. DOI: 10.5194/esd-8-547-2017.
- Matthes, S., Dietmüller, S., Yamashita, H., Soler, M., Simorgh, A., González Arribas, D., Linke, F., Lührs, B., Meuser, M. M., Castino, F. and Yin, F. (2022). "Concept for identifying robust eco-efficient aircraft trajectories." in preparation.
- Matthes, S., Grewe, V., Dahlmann, K., Frömming, C., Irvine, E., Lim, L., Linke, F., Lührs, B., Owen, B., Shine, K., Stromatas, S., Yamashita, H. and Yin, F. (2017). "A Concept for Multi-Criteria Environmental Assessment of Aircraft Trajectories." *Aerospace*, 4(3): 42.
- 720 Matthes, S., Lührs, B., Dahlmann, K., Grewe, V., Linke, F., Yin, F., Klingaman, E. and Shine, K. P. (2020). "Climate-Optimized Trajectories and Robust Mitigation Potential: Flying ATM4E." *Aerospace*, 7(11): 156.
- Methven, J. (1997). *Offline Trajectories: Calculation and Accuracy. Technical Report, UK Universities' Global Atmospheric Modelling Programme*(eds.)].
- 725 Methven, J. (1997). *Offline Trajectories: Calculation and Accuracy. Technical Report, UK Universities' Global Atmospheric Modelling Programme*(eds.)].
- Myhre, G., Nilsen, J. S., Gulstad, L., Shine, K. P., Rognerud, B. and Isaksen, I. S. A. (2007). "Radiative forcing due to stratospheric water vapour from CH₄ oxidation." *Geophysical Research Letters*, 34(1). DOI: <https://doi.org/10.1029/2006GL027472>.
- Myhre, G., Samset, B. H., Schulz, M., Balkanski, Y., Bauer, S., Berntsen, T. K., Bian, H., Bellouin, N., Chin, M., Diehl, T., Easter, R. C., Feichter, J., Ghan, S. J., Hauglustaine, D., Iversen, T., Kinne, S., Kirkevåg, A., Lamarque, J. F., Lin, G., Liu, X., Lund, M. T., Luo, G., Ma, X., van Noije, T., Penner, J. E., Rasch, P. J., Ruiz, A., Seland, Ø., Skeie, R. B., Stier, P., Takemura, T., Tsigaridis, K., Wang, P., Wang, Z., Xu, L., Yu, H., Yu, F., Yoon, J. H., Zhang, K., Zhang, H. and Zhou, C. (2013). "Radiative forcing of the direct aerosol effect from AeroCom Phase II simulations." *Atmospheric Chemistry and Physics*, 13(4): 1853-1877. DOI: 10.5194/acp-13-1853-2013.
- 730 Penner, J. E., Chen, Y., Wang, M. and Liu, X. (2009). "Possible influence of anthropogenic aerosols on cirrus clouds and anthropogenic forcing." *Atmospheric Chemistry and Physics*, 9(3): 879-896. DOI: 10.5194/acp-9-879-2009.
- Rao, P., Yin, F., Grewe, V., Yamashita, H., Jöckel, P., Matthes, S., Mertens, M. and Frömming, C. (2022). "Case Study for Testing the Validity of NO_x-Ozone Algorithmic Climate Change Functions for Optimising Flight Trajectories." *Aerospace*, 9(5): 231.

- 740 Roeckner, E., Brokopf, R., Esch, M., Giorgetta, M., Hagemann, S., Kornblueh, L., Manzini, E., Schlese, U. and Schulzweida, U. (2006). "Sensitivity of Simulated Climate to Horizontal and Vertical Resolution in the ECHAM5 Atmosphere Model." *Journal of Climate*, 19(16): 3771-3791. DOI: 10.1175/jcli3824.1.
- Rosanka, S., Frömming, C. and Grewe, V. (2020). "The impact of weather patterns and related transport processes on aviation's contribution to ozone and methane concentrations from NO_x emissions." *Atmospheric Chemistry and Physics*, 20(20): 12347-12361. DOI: 10.5194/acp-20-12347-2020.
- 745 Sander, R., Jöckel, P., Kirner, O., Kunert, A. T., Landgraf, J. and Pozzer, A. (2014). "The photolysis module JVAL-14, compatible with the MESSy standard, and the JVal PreProcessor (JVPP)." *Geoscientific Model Development*, 7(6): 2653-2662. DOI: 10.5194/gmd-7-2653-2014.
- Sander, R., Kerkweg, A., Jöckel, P. and Lelieveld, J. (2005). "Technical note: The new comprehensive atmospheric chemistry module MECCA." *Atmospheric Chemistry and Physics*, 5(2): 445-450. DOI: 10.5194/acp-5-445-2005.
- 750 Sasaki, D. and Obayashi, S. (2005). "Efficient Search for Trade-Offs by Adaptive Range Multi-Objective Genetic Algorithms." *Journal of Aerospace Computing, Information, and Communication*, 2(1): 44-64. DOI: 10.2514/1.12909.
- Sasaki, D., Obayashi, S. and Nakahashi, K. (2002). "Navier-Stokes optimization of supersonic wings with four objectives using evolutionary algorithm." *Journal of Aircraft*, 39(4): 621-629.
- 755 Schumann, U. and Graf, K. (2013). "Aviation-induced cirrus and radiation changes at diurnal timescales." *Journal of Geophysical Research: Atmospheres*, 118(5): 2404-2421. DOI: doi:10.1002/jgrd.50184.
- Schumann, U., Mayer, B., Graf, K. and Mannstein, H. (2012). "A Parametric Radiative Forcing Model for Contrail Cirrus." *Journal of Applied Meteorology and Climatology*, 51(7): 1391-1406. DOI: 10.1175/jamc-d-11-0242.1.
- 760 Skowron, A., Lee, D. S. and De León, R. R. (2013). "The assessment of the impact of aviation NO_x on ozone and other radiative forcing responses – The importance of representing cruise altitudes accurately." *Atmospheric Environment*, 74: 159-168. DOI: <https://doi.org/10.1016/j.atmosenv.2013.03.034>.
- Sridhar, B., Ng, H. and Chen, N. (2011). "Aircraft Trajectory Optimization and Contrails Avoidance in the Presence of Winds." *Journal of Guidance, Control, and Dynamics*, 34(5): 1577-1584. DOI: 10.2514/1.53378.
- 765 Stevenson, D. S., Doherty, R. M., Sanderson, M. G., Collins, W. J., Johnson, C. E. and Derwent, R. G. (2004). "Radiative forcing from aircraft NO_x emissions: Mechanisms and seasonal dependence." *Journal of Geophysical Research: Atmospheres*, 109(D17). DOI: <https://doi.org/10.1029/2004JD004759>.

- Szopa, S., Naik, V., Adhikary, B., Artaxo, P., Berntsen, T., Collins, W. D., Fuzzi, S., Gallardo, L., Kiendler-Scharr, A., Z. Klimont, Liao, H., Unger, N. and Zanis, P. (2021). Short-Lived Climate Forcers. In *Climate Change 2021: The Physical Science Basis. Contribution of Working Group I to the Sixth Assessment Report of the Intergovernmental Panel on Climate Change*. [V. Masson-Delmotte, P. Zhai, A. Pirani, S. L. Connors, C. Péan, S. Berger, N. Caud, Y. Chen, L. Goldfarb, M. I. Gomis, M. Huang, K. Leitzell, E. Lonnoy, J. B. R. Matthews, T. K. Maycock, T. Waterfield, O. Yelekçi, R. Yu and B. Zhou (eds.)]. Cambridge University Press, Cambridge, United Kingdom and New York, NY, USA, pp.817-922. DOI: <https://doi.org/10.1017/9781009157896.008>.
- 770 Terrenoire, E., Hauglustaine, D. A., Cohen, Y., Cozic, A., Valorso, R., Lefèvre, F. and Matthes, S. (2022). "Impact of present and future aircraft NO_x and aerosol emissions on atmospheric composition and associated direct radiative forcing of climate." *Atmos. Chem. Phys.*, 22(18): 11987-12023. DOI: 10.5194/acp-22-11987-2022.
- 775 Tost, H. (2006). Global Modelling of Cloud, Convection and Precipitation Influences on Trace Gases and Aerosols PhD thesis, University of Bonn.
- Tost, H., Jöckel, P., Kerkweg, A., Sander, R. and Lelieveld, J. (2006a). "Technical note: A new comprehensive SCAVenging submodel for global atmospheric chemistry modelling." *Atmospheric Chemistry and Physics*, 6(3): 565-574. DOI: 10.5194/acp-6-565-2006.
- 780 Tost, H., Jöckel, P. and Lelieveld, J. (2006b). "Influence of different convection parameterisations in a GCM." *Atmospheric Chemistry and Physics*, 6(12): 5475-5493. DOI: 10.5194/acp-6-5475-2006.
- Tost, H., Jöckel, P. and Lelieveld, J. (2007). "Lightning and convection parameterisations & uncertainties in global modelling." *Atmospheric Chemistry and Physics*, 7(17): 4553-4568. DOI: 10.5194/acp-7-4553-2007.
- 785 van Manen, J. and Grewe, V. (2019). "Algorithmic climate change functions for the use in eco-efficient flight planning." *Transportation Research Part D: Transport and Environment*, 67: 388-405. DOI: <https://doi.org/10.1016/j.trd.2018.12.016>.
- Voigt, C., Lelieveld, J., Schlager, H., Schneider, J., Curtius, J., Meerkötter, R., Sauer, D., Bugliaro, L., Bohn, B., Crowley, J. N., Erbetseder, T., Groß, S., Hahn, V., Li, Q., Mertens, M., Pöhlker, M. L., Pozzer, A., Schumann, U., Tomsche, L., Williams, J., Zahn, A., Andreae, M., Borrmann, S., Brüner, T., Dörich, R., Dörnbrack, A., Edtbauer, A., Ernle, L., Fischer, H., Giez, A., Granzin, M., Grewe, V., Harder, H., Heinritzi, M., Holanda, B. A., Jöckel, P., Kaiser, K., Krüger, O. O., Lucke, J., Marsing, A., Martin, A., Matthes, S., Pöhlker, C., Pöschl, U., Reifenberg, S., Ringsdorf, A., Scheibe, M., Tadic, I., Zauner-Wieczorek, M., Henke, R. and Rapp, M. (2022). "Cleaner Skies during the COVID-19 Lockdown." *Bulletin of the American Meteorological Society*, 103(8): E1796-E1827. DOI: 10.1175/bams-d-21-0012.1.

- 795 Wilcox, L. J., Shine, K. P. and Hoskins, B. J. (2012). "Radiative forcing due to aviation water vapour emissions." *Atmospheric Environment*, 63: 1-13. DOI: <https://doi.org/10.1016/j.atmosenv.2012.08.072>.
- Wild, O., Prather, M. J. and Akimoto, H. (2001). "Indirect long-term global radiative cooling from NO_x Emissions." *Geophysical Research Letters*, 28(9): 1719-1722. DOI: <https://doi.org/10.1029/2000GL012573>.
- Winterstein, F. and Jöckel, P. (2021). "Methane chemistry in a nutshell – the new submodels CH₄ (v1.0) and TRSYNC (v1.0) in MESSy (v2.54.0)." *Geoscientific Model Development*, 14(2): 661-674. DOI: 10.5194/gmd-14-661-2021.
- 800 WMO (1957). "Definition of the tropopause." *WMO Bull.*, 6: 136.
- Yamashita, H., Grewe, V., Jöckel, P., Linke, F., Schaefer, M. and Sasaki, D. (2016). "Air traffic simulation in chemistry-climate model EMAC 2.41: AirTraf 1.0." *Geoscientific Model Development* 9: 3363–3392. DOI: <https://doi.org/10.5194/gmd-9-3363-2016>.
- 805 Yamashita, H., Yin, F., Grewe, V., Jöckel, P., Matthes, S., Kern, B., Dahmann, K. and Frömming, C. (2020). "Newly developed aircraft routing options for air traffic simulation in the chemistry–climate model EMAC 2.53: AirTraf 2.0." *Geoscientific Model Development*, 13: 4869–4890. DOI: <https://doi.org/10.5194/gmd-13-4869-2020>.
- Yin, F., Grewe, V., Frömming, C. and Yamashita, H. (2018). "Impact on flight trajectory characteristics when avoiding the formation of persistent contrails for transatlantic flights." *Transportation Research Part D: Transport and Environment*, 65: 466-484. DOI: <https://doi.org/10.1016/j.trd.2018.09.017>.
- 810

Appendix A list of EMAC submodels used in the chemistry simulation

Table A.1 Summary of MESSy submodels used in the chemistry simulation.

Submodel	Purpose	Reference
AEROPT	Aerosol optical properties for the radiation scheme	Dietmüller et al., 2016
ACCF 1.0	Climate impact of aviation emissions and contrails calculation	Section 3 of this article
AIRTRAF 2.0	Air traffic simulation	Yamashita et al., 2020
CH4 1.0	Simple methane chemistry	Winterstein and Jöckel, 2021
CLOUD	Standard ECHAM5 cloud microphysics calculation	Roeckner et al., 2006
CLOUDOPT	Cloud optical properties calculation for the radiation scheme	Dietmüller et al., 2016
CVTRANS	Calculates the transport of tracers due to convection	Tost, 2006
CONVECT	Convection process calculation	Tost et al., 2006b
CONTRAIL	Contrail potential coverage calculation	Supplement of Grewe et al., 2014a; Yin et al., 2018
DDPE	Dry deposition of gas phase and aerosol tracers	Kerkweg et al., 2006a
E5VDIFF	ECHAM5 vertical diffusion and land-atmosphere exchange	Jöckel et al., 2010
GWAVE	Gravity waves calculation	Jöckel et al., 2010
JVAL	Photolysis rates	Sander et al., 2014
LNOX	Lighting NO _x production	Tost et al., 2007
MSBM	Multi-phase stratospheric box model calculates the heterogeneous reaction rates on polar stratospheric cloud particles and stratospheric background aerosols	Jöckel et al., 2010
MECCA	Calculates tropospheric and stratospheric chemistry	Sander et al., 2005
O3ORIG	To trace the origin of ozone	Grewe, 2006
OFFEMIS	Prescribed emissions of trace gases and aerosols	Kerkweg et al., 2006b
ONEMIS	Online calculated emissions of trace gases and aerosols	Kerkweg et al., 2006b
ORBIT	Earth orbit calculation for solar zenith angle, etc.	Dietmüller et al., 2016
RAD	Simulates the radiative flux	Dietmüller et al., 2016
SCAV	Simulates the process of wet deposition and liquid phase chemistry.	Tost et al., 2006a
SCAL	Simple calculations with channel objects to separate the AirTraf ozone from other ozone sources	Jöckel et al., 2010
SEDI	Sedimentation of aerosol particles	Kerkweg et al., 2006a
SURFACE	Calculates the surface temperature	Jöckel et al., 2010

TAGGING 1.0	Tag the emissions contributions to concentrations	Grewe et al., 2017a
TNUDGE	Tracer nudging	Kerkweg et al., 2006b
TROPOP	Tropopause and other diagnosis	Jöckel et al., 2006
VISO	Vertically layered iso-surfaces and maps	Jöckel et al., 2010

815